Clim Dyn (2013) 41:1385–1405
DOI 10.1007/s00382-013-1696-x

ORIGINAL ARTICLE

A decadal microwave record of tropical air temperature from AMSU-A/aqua observations

Yuan Shi · King-Fai Li · Yuk L. Yung · Hartmut H. Aumann · Zuoqiang Shi · Thomas Y. Hou

Received: 6 June 2012 / Accepted: 4 February 2013 / Published online: 27 February 2013

Abstract Atmospheric temperature is one of the most important climate variables. This observational study presents detailed descriptions of the temperature variability imprinted in the 9-year brightness temperature data acquired by the Advanced Microwave Sounding Unit-Instrument A (AMSU-A) aboard Aqua since September 2002 over tropical oceans. A non-linear, adaptive method called the Ensemble Joint Multiple Extraction has been employed to extract the principal modes of variability in the AMSU-A/Aqua data. The semi-annual, annual, quasi-biennial oscillation (QBO) modes and QBO–annual beat in the troposphere and the stratosphere have been successfully recovered. The modulation by the El Niño/Southern oscillation (ENSO) in the troposphere was found and correlates well with the Multivariate ENSO Index. The long-term variations during 2002–2011 reveal a cooling trend (−0.5 K/decade at 10 hPa) in the tropical stratosphere; the trend below the tropical tropopause is not statistically significant due to the length of our data. A new tropospheric near-annual mode (period ∼1.6 years) was also revealed in the troposphere, whose existence was confirmed using National Centers for Environmental Prediction Reanalysis air temperature data. The near-annual mode in the troposphere is found to prevail in the eastern Pacific region and is coherent with a near-annual mode in the observed sea surface temperature over the Warm Pool region that has previously been reported. It remains a challenge for climate models to simulate the trends and principal modes of natural variability reported in this work.

Keywords Atmospheric variability · Principal mode decomposition · Adaptive analysis · Amplitude and phase profiles · Near-annual variability · Temperature trends

Electronic supplementary material The online version of this article (doi:10.1007/s00382-013-1696-x) contains supplementary material, which is available to authorized users.

Y. Shi
Department of Physics, The University of Hong Kong, Pokfulam, Hong Kong

Present Address:
Y. Shi
Princeton Plasma Physics Laboratory, Department of Astrophysical Sciences, Princeton University, Princeton, NJ, USA

K.-F. Li (✉) · Y. L. Yung
Division of Geological and Planetary Sciences, California Institute of Technology, Pasadena, CA, USA
e-mail: kfl@gps.caltech.edu

H. H. Aumann
Jet Propulsion Laboratory, California Institute of Technology, Pasadena, CA, USA

Z. Shi · T. Y. Hou
Applied and Computational Mathematics, California Institute of Technology, Pasadena, CA, USA

Present Address:
Z. Shi
Mathematical Sciences Centre, Tsinghua University, Beijing, China

1 Introduction

Temperature in the lower atmosphere (here we refer to the troposphere and the stratosphere) has been one of the most important climate variables in the study of climate change (Allen et al. 2006; Broecker 1975; IPCC 1990, 2007). Its variations affect many aspects of the earth system, including the hydrological cycle (Ramanathan et al. 2001),

the sea level (Wigley and Raper 1992), glaciers (Haeberli et al. 1999), the arctic ice cap (Dowdeswell et al. 1997) and the ecological system (Bergengren et al. 2011; Hughes et al. 2003). Comprehensive knowledge of both natural and human-induced variations in the atmospheric temperature and how these variations are coupled to other terrestrial components are thus crucial for predicting the future climate.

The lower atmospheric temperature has been monitored from ground by in situ measurements or remote sensing techniques such as lidar and from space since 1970s. A great advantage of spaceborne measurements is their global coverage on daily basis. Our interest is in the spaceborne temperature data. There have been efforts to construct a continuous temperature record for climate studies using successive satellite measurements (Christy et al. 2007). However, differences in the instrumental calibrations and drifts may lead to artificial fluctuations/trends in the composite records (Xu and Powell 2012). Our aim is to seek a high-quality long-term temperature record from a single, stable satellite instrument such that the aforementioned artifacts/instrumental uncertainties can be avoided. In this paper, we will use as an example the temperature data acquired by the Advanced Microwave Sounding Unit-Instrument A (AMSU-A; Lambrigtsen 2003) aboard the National Aeronautics and Space Administration's (NASA's) Earth Observing System (EOS) Aqua satellite (Aumann et al. 2003) since its launch in 2002. Our aim is to document in details the temperature variability imprinted in the 9-year AMSU-A/Aqua data during 2002–2011.

AMSU-A/Aqua is one of the A-Train satellite instruments (L'Ecuyer and Jiang 2010) in the EOS that provides an accurate and complete set of measurements of variables believed to be crucial for the climate system. Using microwave between 23 and 89 GHz, AMSU-A is capable of obtaining accurate temperature measurements for the troposphere and stratosphere even in the presence of cloud (Susskind et al. 2003). The AMSU-A/Aqua data constitute the longest data period of microwave sounding available from a single instrument in an accurately maintained polar orbit. The Aqua spacecraft was launched in May 2002. The Aqua polar orbit is actively maintained within 30 s for a 1:30 p.m. ascending node equator crossing at 705 km altitude, which effectively eliminates the cross-talk with the diurnal cycle and minimizes the orbital drift problem. As of May 2002, AMSU-A/Aqua provides the longest time series of microwave measurements from a single instrument in support of climate analysis. We note that, the previous AMSU-A on the National Oceanic and Atmospheric Administration (NOAA)-15 satellite, launched in 1998 into polar orbit, was the first of a new generation of total power microwave radiometers. Unfortunately, since the orbit of NOAA-15 was not actively controlled, the ascending node of its orbit shifted between 1998 and 2007 from 7:30 p.m. to 5 p.m. local time. This introduced diurnal cycle artifacts in the time series (Mo 2009). Thus AMSU-A/NOAA-15 data will not be used in this paper. AMSU-A has also been installed on the European satellite MetOp-A, which was launched into the orbit in 2006. This record is a few years shorter than that of AMSU-A/Aqua and will not be used here.

There are fifteen microwave channels on AMSU-A/Aqua. Ten of them (Channel 5–14) that are relatively insensitive to the surface conditions will be examined in this paper. Each of these channels has sensitivity to atmospheric temperature variations at different altitudes between 2.5 and 700 hPa. Thus, combining these temperature measurements provides the vertical profile of temperature variations during the last decade, which contains the information about vertical propagations that may be used for diagnosis of current climate models.

We will decompose the decadal temperature record from AMSU-A/Aqua into a long-term trend and intrinsic modes of variability and to construct vertical patterns associating with them. Such a decomposition is useful for climate studies because we are always interested in separating the small secular trend ($\leq$1 K/decade), primarily caused by the increase of greenhouse gases, from other variability, e.g. the seasonal cycle ($\sim$10 K), the quasi-biennial oscillation (QBO; $\sim$few K), and quasi-periodic changes due to the El Niño/Southern oscillation (ENSO; Wang and Picaut 2004). A common approach of time series decomposition is to use linear parametric methods such as the Fourier transform or a simple running-average filter to isolate different modes of variability. An advantage of using these parametric methods is that the filtered data can be easily interpreted in terms of the physical meanings of the chosen parameters. However, a minimal knowledge about the underlying system is required to determine the values of the parameters. In addition, the underlying system has to be linear and stationary, which is generally not true for real data.

There have been growing interests in developing adaptive methods that decompose a non-linear time series based only on the nature of the time series *per se*, in the way that the decomposition does not require any assumptions or prior information. Examples of such adaptive methods include the Empirical Mode Decomposition (EMD) (Huang et al. 1998), the Hilbert spectral representation based on wavelet projection (Olhede and Walden 2004), and the synchrosqueezed wavelet transforms (Daubechies et al. 2011; Wu et al. 2011). Recently, Hou and Shi (2011) developed a more mathematically-based version of EMD, tentatively named the Decomposition Matching Pursuit (DMP), which treats EMD as a nonlinear L^1 optimization problem. Based on the examples given in Hou and Shi (2011), DMP shows similar properties as of EMD and preserves the intrinsic properties of the input signal (such as trends and instantaneous frequency). It is also less

sensitive to noise perturbation, which seem to be the major weakness of EMD. However, as will be discussed below, DMP also subjects to the problem of end-point problem. In this paper, we will decompose the AMSU-A/Aqua data using DMP, with appropriate treatments of the end-point problem using the ensemable EMD (EEMD; Wu and Huang 2009); the combined DMP-EEMD method will be called the Ensemble Joint Multiple Extraction (EJME).

The rest of the paper is organized as follows. The AMSU-A/Aqua data are described in Sect. 2, followed by a brief description of the principal method used in our data analysis in Sect. 3. The results are presented in Sect. 4, where an overview of the monthly-averaged raw data is first given, followed by discussions of the principal modes extracted by EJME. In Sect. 5, the principal modes of similar periods are combined to give a time–height picture of their vertical propagations. Long-term variations represented by the last principal modes are also presented. Finally, we will report a less-known near-annual mode in the troposphere, which we will relate to a near-annual mode in the sea surface temperature (SST) in the Warm Pool region. Section 6 summarizes the main findings in this work. A detailed description of our principal method is given in "Appendixes 2 and 3".

2 Data

2.1 AMSU-A/aqua brightness temperature

The tropically averaged (30°S–30°N) brightness temperature (T_B) over ocean measured by Channels 5–14 of AMSU-A/Aqua will be used in this study. (Channel 4 stopped functioning since 2006 and the other channels are sensitive to the surface conditions.) These channels are relatively insensitive to surface conditions (Goldberg et al. 2001) and the presence of clouds (Susskind et al. 2003). The AMSU-A/Aqua data constitute the longest data period of microwave sounding available from a single instrument in an accurately maintained polar orbit. Aqua was launched into a polar sun-synchronous orbit in May 2002 at 705 km altitude. AMSU-A/Aqua scans ±49° cross track with 3.3° (40.6 km at nadir) diameter footprints (Lambrigtsen 2003). The AMSU-A/Aqua observations have considerable zenith angle dependence, and to avoid errors introduced by limb adjustment, we use only near-nadir observations in this paper.

Each day since 1 September, 2002, AMSU-A/Aqua generates ~0.5 million measurements, which corresponds to ~100 MB of calibrated radiances from Channels 5–14. In order to manage this data volume, we randomly collect ~3,400 samples within 3° of nadir from the tropical oceans (30°S–30°N) during the 1:30 a.m. local overpasses, referred to as "night" and an approximately equal number of samples from the 1:30 p.m. overpass referred to as "day". This random selection is described in details in "Appendix 1". An example of the daily spatial distribution of data is shown in Fig. 11a. The daily means of AMSU-A/Aqua radiances are calculated for each calendar day between 30°S and 30°N. Of the 3,287 days between 1 September, 2002 and 31 August, 2011, 50 days of data are missing due to various spacecraft and downlink problems. The missing days are filled by sinusoidal functions before obtaining the monthly averaged data, which will be used in this study.

The weighting functions of AMSU/Aqua Channels 5–14 spread over some altitude range (~10 km) and peak at different pressure levels/altitudes from the mid-troposphere to the mid-stratosphere. For example, over tropical oceans, Channel 5 measures the mid-tropospheric temperature at ~700 hPa, Channel 9 around the tropopause temperature at ~90 hPa, and Channel 14 the mid-stratospheric temperature at ~2.5 hPa. The weighting functions of the AMSU-A/Aqua channels at near-nadir view can be found from Fig. 7 of Goldberg et al. (2001). Approximate peak pressures/altitudes as well as the full width at half maximum (FWHM) for Channels 5–14 are listed in Table 1.

2.2 Air temperature and sea surface temperature

To help confirm the existence of some extracted IMFs (the near-annual modes that will be discussed in Sect. 5), we will use the air temperature data assimilated in the National Centers for Environmental Prediction Reanalysis-I (NCEP-1) (Kalnay et al. 1996). The NCEP-1 data are given on 17 pressure levels between 10 and 1,000 hPa and has a horizontal resolution of 2.5° × 2.5°. The NCEP-1 daily data

Table 1 Approximate pressure/altitudes levels to which the AMSU-A/Aqua Channels 5–14 are most sensitive and the full width at half maximum (FWHM) of the weighting functions

Channel no.	Peak level		FWHM	
	Pressure (hPa)	Altitude (km)	Pressure (hPa)	Altitude (km)
5	700	3	750	10
6	400	8	500	10
7	250	11	400	10
8	150	14	240	10
9	90	17	120	9
10	50	20	80	10
11	25	25	40	10
12	10	31	20	11
13	5	37	8	12
14	2.5	41	4	12

The weighting functions of AMSU-A channels at near nadir view are shown in Fig. 7 of Goldberg et al. (2001)

after 2002 will be used and these data are averaged monthly.

The daily sea surface temperature (SST) from the Tropical Rainfall Measuring Mission (TRMM) Microwave Imager (TMI) will also be used (Reynolds et al. 2010). TMI SST data are retrieved from the microwave channel 10.7 GHz, which is nearly transparent to clouds. The measurements are available since 1997 but only the SST data after 2002 will be used in the study. The TMI SST data has a spatial resolution of 0.25° × 0.25°. However, our focus is on relatively large-scale variability in the SST. So the TMI SST have been averaged monthly onto a coarser resolution of 2.5° in latitudes.

3 Methods

3.1 Decomposition matching pursuit (DMP)

By defining the "smoothness" of a function as the third-order total variation (TV^3):

$$TV^3[g(t)] = \int_a^b \left|\frac{d^4 g(t)}{dt^4}\right| dt, \tag{1}$$

DMP decomposes a time series $f(t)$ into a sum of the smallest number of intrinsic mode functions (IMFs) of the form $a(t)\cos[\theta(t)]$, where $a(t) > 0$ is assumed to be smoother than $\cos[\theta(t)]$ and (t) is a piecewise smooth increasing function (i.e. $\frac{d\theta(t)}{dt} \geq 0$). In other words, it looks for decomposition.

$$f(t) = \sum_{k=1}^{M} a_k(t)\cos[\theta_k(t)] \tag{2}$$

where M is minimized. The above definition of IMF by Hou and Shi (2011) is a mathematical generalization of that defined by Huang et al. (1998). Note that EMD also decomposes $f(t)$ into the form of Eq. (2) but M is not necessarily minimized.

(a) Iterative decomposition for ideal data without noise

Hou and Shi (2011) propose a recursive approach to solve for $a_k(t)$ and $\theta_k(t)$. Consider a time series $f(t)$ without noise. We seek the highest-frequency IMF $a_1(t)\cos[\theta_1(t)]$ using a Newton-type iterative method such that the remainder $f_1(t) = f(t) - a_1(t)\cos[\theta_1(t)]$ is the smoothest. To do this, an initial guess of $\theta_1^0(t)$ is required; in the absence of noise, $\cos[\theta_1^0(t)]$ can be taken as the shifted/normalized $f(t)$ such that all maxima equal $+1$ and all minima equal -1. Next, we find some functions $f_1^0(t)$, $a_1^0(t)$, and $b_1^0(t)$ such that the sum of their total variations $TV^3[f_1^0(t)] + TV^3[a_1^0(t)] + TV^3[b_1^0(t)]$ is minimized while $f_1^0(t) + a_1^0(t) + b_1^0(t)\sin[\theta_1^0(t)] = f(t)$. The minimization is done through the split Bregman iteration (Goldstein and Osher 2009). If the L_2-norm $\left\|\tan^{-1}\left(b_1^0/a_1^0\right)\right\|_2$ is greater than some threshold ε_0, then we improve the estimate of the phase function by taking $\theta_1^1(t) = \theta_1^0(t) - \mu\tan^{-1}\left(b_1^0/a_1^0\right)$, where μ is the largest value between 0 and 1 such that $\theta_1^1(t)$ is piecewise increasing, and repeat the above minimization to obtain $f_1^1(t)$, …, $f_1^n(t)$, $a_1^1(t)$, …, $a_1^n(t)$, and $b_1^1(t)$, …, $b_1^n(t)$ until $\left\|\tan^{-1}\left(b_1^n/a_1^n\right)\right\|_2 \leq \varepsilon_0$. The final $f_1^n(t)$ is the required remainder $f_1(t)$. In the similar fashion, $f_1(t)$ can then be decomposed further: $f(t) = f_1(t) + a_1(t)\cos[\theta_1(t)] = f_2(t) + a_2(t)\cos[\theta_2(t)] + a_1(t)\cos[\theta_1(t)] = \cdots$. As a result, $f(t)$ is decomposed into the form of Eq. (2) recursively.

(b) Iterative decomposition for real data with noise

For real data in the presence of noise, the above shifting–normalization scheme for estimating $\cos[\theta_k^0(t)]$ does not work. Instead, $\cos[\theta_k^0(t)]$ is taken as the band-pass filtered time series by Fourier transform with the band-pass frequencies embracing the highest frequency component in $f_k(t)$. However, an initial guess of the band-pass frequencies have to be supplied, which requires a visual determination from the raw Fourier spectrum that has to be done manually. $\theta_k^0(t)$ (the arc-cosine of the bass-pass filtered time series) so estimated may subject to some end-point problems, the treatment of which will be discussed in the next subsection. In addition, $f_k(t)$ has to be "regularized" before the TV^3 minimization: given the nth iterative estimate $\overset{n}{k}(t)$, we regard as noise the variability of $f_k(t)$ that have higher frequencies than those of $\cos[\theta_k^n(t)]$ and remove them from $f_k(t)$. This regularization is done by first transforming the independent variable of f_k from t to θ_k^n. Then the Meyer low-pass filter $\Psi(v_\theta)$ is applied to the Fourier transform $\mathcal{F}\left[f_k\left(\theta_k^n\right)\right]$ of $f_k(\theta_k^n)$ to remove variability of frequencies higher than one wavenumber, where v is the wavenumber in the Fourier space of θ_k^n, and

$$\Psi(v_\theta) = \begin{cases} 1, & |v_\theta| \leq 1 \\ \frac{1}{2}\left[1 - \cos(\pi v_\theta)\right], & 1 \leq |v_\theta| \leq 2. \\ 0, & v_\theta \geq 2 \end{cases} \tag{3}$$

The low-pass filtered time series $\bar{f}_k\left(\theta_k^n\right) = \mathcal{F}^{-1}\left\{\mathcal{F}\left[f_k\left(\theta_k^n\right)\right]\Psi(v_\theta)\right\}$ is transformed back to $\bar{f}_k(t)$ and the DMP can then be applied.

3.2 The end-point problem and the ensemble joint multiple extraction (EJME)

As discussed in Sect. 3.1, when noise is present, a Fourier transform filtering has been used to generate $\cos[\theta_k^0(t)]$ that is confined within some frequency range. Such a treatment effectively avoids the notorious scale mixing problem in

EMD, which makes the physical meaning of modes obscure. However, because of the Fourier transform, DMP inherits the end-point problem when it periodically extends the time series. Hence in our analysis, the EEMD, which is a noise-assisted version of EMD, is jointly used with DMP to resolve the end-point problem. It should be noted that using cubic spline fitting, EEMD also has its end-point problem, but it is significantly less serious than that of EMD (Wu and Huang 2009).

A detailed description of the treatment of the end-point problem can be found in "Appendix 2". Here we briefly summarize the procedures. Whenever necessary, data are first masked to ensure that modes will not be strongly distorted by highly asymmetric events like stratospheric sudden warming (SSW). After the DMP decomposition, EEMD is employed to extract the remaining signals near the ends of the time series. The IMFs extracted by EEMD are masked by a plateau-like weighting function and are then combined with IMFs extracted by DMP whenever they are found to have similar frequency components. After this, residuals from DMP and EEMD are combined to become time series used for the next round of extraction. This process is repeated multiple times to ensure complete extraction. In the next step, EEMD is employed multiple times to extract low-frequency signals from the residual. The last IMF is taken as the summation of all the low-frequency IMFs, and the trend is taken as the EEMD trend from the last round of extraction. Finally, highly asymmetric events, if any, are combined with the residual to become the final residual labeled as IMF1. Modes obtained by such treatment are well separated with little scale mixing, and trends obtained by such treatment can effectively avoid the strong influence of the asymmetric ENSO and SSW.

To give an estimation of the uncertainty of the IMFs, an ensemble of decompositions is performed by adding white noises to data. In our analysis, the ensemble number is typically taken to be 1,000. Each noise-added time series is decomposed using the combined DMP/EEMD described above. The ensemble means of the DMP/EEMD modes will be taken as the final decomposition in the following discussions. The 1-σ standard deviations of the ensemble decompositions give an estimation of the statistical significance of the decomposition. Since IMF 1 is usually noise (except in good cases like Channel 9; see Sect. 4.2), in our analysis the input noise level is chosen to be the standard deviation of the masked IMF 1 of the original time series. Technical details of EJME are presented in "Appendix 2".

3.3 Amplitudes and phases

The amplitude of an IMF is defined by its standard deviation because the IMFs may be irregular and not perfectly harmonic. The phase difference between two time series will be defined as the averaged difference in time when the local maxima of the respective time series occur; a more mathematical definition of the occurrence time of a local maximum is given in "Appendix 3".

4 Results

As discussed in Introduction, our aim is to study the richness of the T_B variability imprinted in currently the longest record of microwave measurements by AMSU-A/Aqua. Below, we will first present the general features of the monthly averages (Sect. 4.1). Then we will present the decomposed IMFs by EJME (Sect. 4.2). Note that the analyses below use T_B over tropical oceans only.

4.1 Monthly averages

The monthly-averaged time series for AMSU-A/Aqua Channels 5–14 are plotted in Fig. 1a. Their Fourier spectra, which have been used for estimating $\cos[\theta_k^0(t)]$, are displayed to their right in Fig. 1b. The dotted, dashed and the dash-dotted lines are the 99, 95, and 90 % confidence levels, respectively. The power spectra are normalized such that the total area under each spectrum equals the variance of its corresponding time series.

Channel 5 is most sensitive to T_B variations in the lower troposphere near 700 hPa (Table 1). The peak-to-trough variability acquired by this channel is $\sim$1 K. Its Fourier spectrum has a significant peak at 1 year, which is due to the annual cycle. The spectrum also has a broad peak for periods 3–5 years, which is likely due to the ENSO. There is a peak at $\sim$1.6 years, which is significant at a 95 % confidence level. This may be due to a less-known near-annual mode in the SST (Jin et al. 2003), which then modulates the air temperature near the ocean surface. We will discuss some possible mechanisms responsible for this near-annual mode in Sect. 5.5. The T_B time series acquired by Channels 6 (corresponding to variations in the mid-troposphere at 400 hPa) is very similar to that acquired by Channel 5, with a peak-to-trough variability of $\sim$1 K. The spectral peaks of the annual cycle, the near-annual mode, and the ENSO are also apparent.

Channels 7–8 and 9–10 are most sensitive to the T_B variations in the tropical tropopause region between 150 and 250 hPa and the lower stratosphere region between 50 and 90 hPa, respectively. In both of the regions, the annual cycles are the most dominant, having a peak-to-trough amplitude of 3–4 K. The effects of the near-annual cycle and the ENSO here are relatively weak compared to the annual variability and are not apparent without filtering.

Moving to the middle stratosphere (10–25 hPa), where the T_B variations are effectively measured by Channels 11 and 12, the annual cycle also shows an amplitude of 3–4 K. In addition, a semi-annual oscillation (SAO) becomes apparent, which has amplitude a few times smaller than that of the annual cycle. From the T_B variations in the upper stratosphere (2.5–5 hPa) measured by Channels 13 and 14, the SAO completely dominates while the annual cycle becomes the second dominant T_B variability; the overall amplitude of the T_B variability is again 3–4 K.

It should be noted that the effects of QBO, which is the most dominant form of the inter-annual variability in the tropical stratosphere, are not apparent in these spectra. Therefore, certain filtering techniques are required to observe the effects of QBO, as we will do in the next section using EJME.

We also note that the tropically-averaged T_B from Channels 5–8 all show variability of amplitudes within ±1.5 K. Therefore the tropical troposphere and tropopause are amazingly stable in terms of T_B.

4.2 EJME decomposition

EJME is employed to separate weak signals (e.g. QBO) from other dominant signals (e.g. the seasonal cycle).

In Fig. 2a, the monthly-averaged time series of T_B acquired by AMSU-A/Aqua Channel 5 is shown at the top. The IMFs obtained by the EJME decomposition are shown below. In each figure, the black line is the ensemble mean and the shaded area is 1-σ ensemble deviation. The FFT spectra are displayed on the right in Fig. 2b. IMF 1 (residual of the EJME decomposition) appears to be a high-frequency mode, which in this case is mostly noise. IMF 2 is a mixture of the SAO and some high-frequency components; the large ensemble deviation indicates that the SAO is not well established in the troposphere. IMF 3 is the

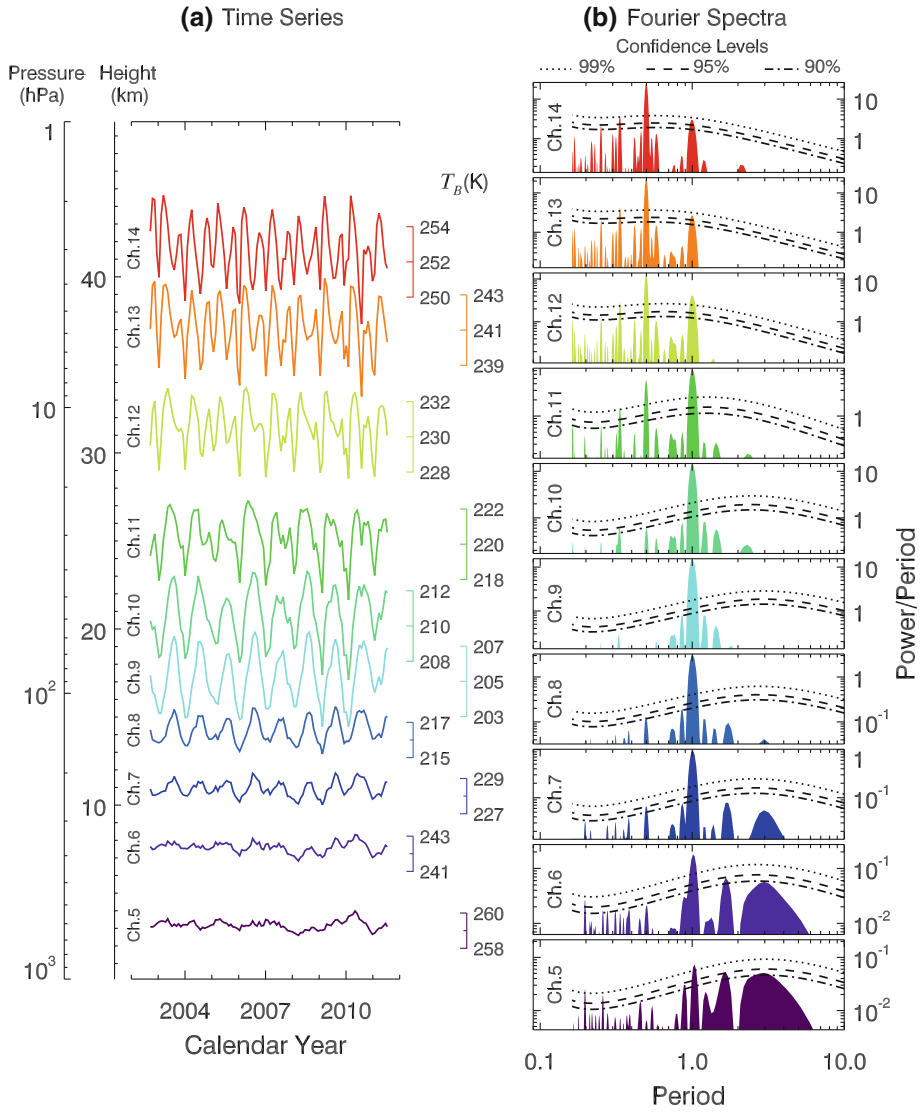

Fig. 1 **a** Raw monthly-averaged brightness temperature (T_B) acquired by Channels 5–14 of AMSU-A/Aqua. Each channel is sensitive to a different altitude/pressure level, which is shown on the *left*. **b** The Fourier spectra of the time series. The *dotted*, *dashed*, and *dash-dotted lines* are the 99, 95, and 90 % confidence levels, respectively. The period is in unit of years. The time series have been padded with zeros before the spectra are obtained such that total length of the time series becomes 2^{n+2}, where n is the smallest power of 2 that is greater than or equal to the original number of time steps

annual cycle. IMF 4 is the near-annual variability with a single peak at ~1.6 years in its spectrum. IMF 5 has a period of 2–3 years and IMF 6 has a period of 3–6 years. Finally, IMF 7 at the bottom of Fig. 2a represents the overall trend during 2002–2011. It shows a 9-year cooling trend of -0.1 ± 0.1 K/decade. The statistical significance of this cooling trend (as well as the trends at other altitudes) will be discussed further in Sect. 5.4.

Both IMFs 5–6 characterize an inter-annual variability in the troposphere which is likely related to the ENSO. To verify this, the sum of IMFs 5–6 (blue solid line) is compared to the Multi-variate ENSO Index (MEI; red/orange shades; Wolter and Timlin 2011) in Fig. 2c. In 2002–2007, there is a weak persistent El Niño (i.e. warming) event in the eastern Pacific, indicated by the small oscillating positive MEI values, except for a short period at the end of 2005, where the MEI shows a small negative value, representing a weak La Niña (i.e. cooling) event in the eastern Pacific during that period. The strong La Niña events in 2008 and 2010–2011 and the strong El Niño event in 2009 are apparent in the MEI index. The variations of the MEI index are well reflected in the sum of IMFs 5–6, except that the cooling during 2010 seems to have occurred ~5 months later (when the cross-correlation is maximized). However, it is not clear whether the 5-month lag is physical.

The application of EJME to the T_B data acquired by Channels 6–8 yields similar IMFs (Figs. S1–S3), with IMFs having different amplitudes and relative phases that will be discussed in Sect. 5. Similar to those of Channel 5,

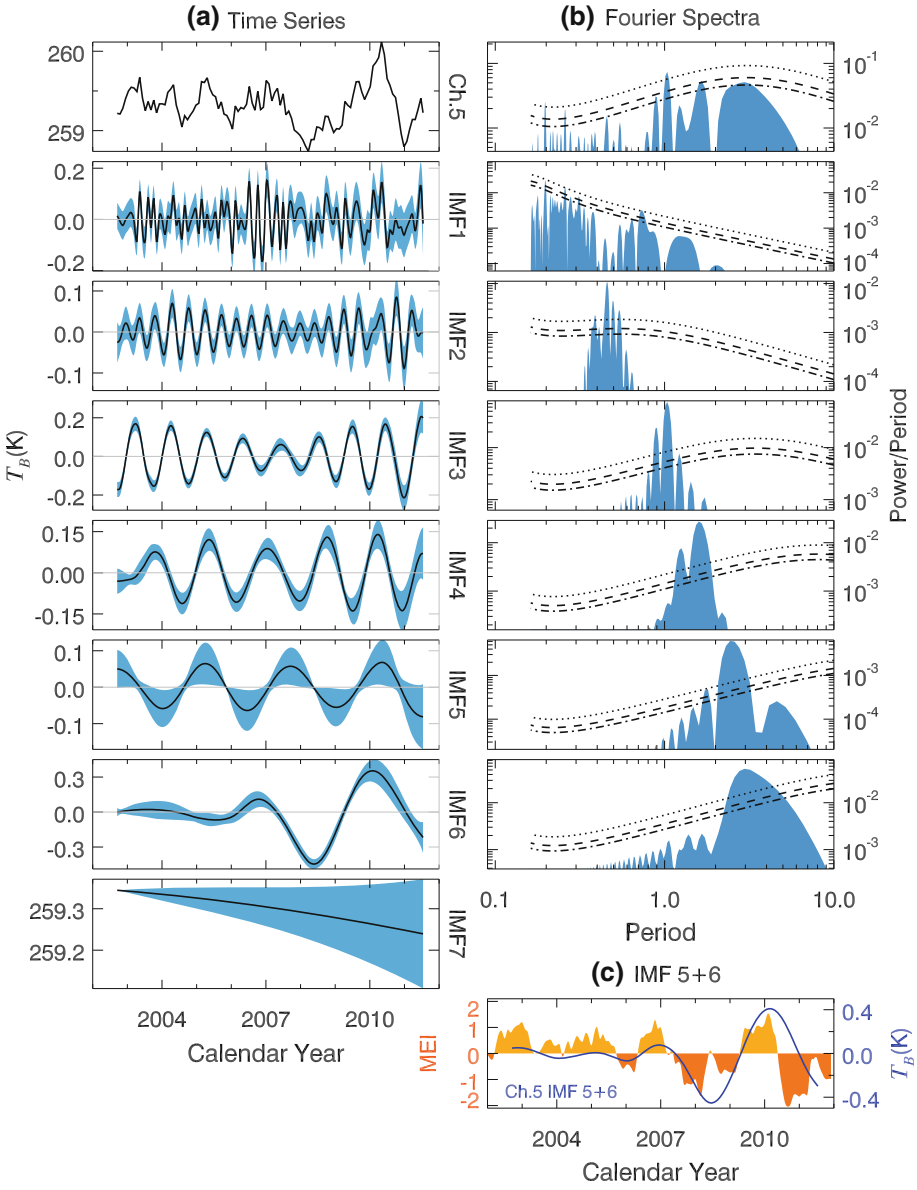

Fig. 2 **a** The IMFs of T_B measured by AMSU-A/Aqua Channel 5. The raw monthly-averaged time series is shown at the *top*. Modes and trend are listed underneath. The *solid lines* are the means of the ensemble decomposition and the *shaded areas* are the 1-σ ensemble deviations. **b** Fourier spectra for ensemble means. The area under curves equals the variance of the time series. The period is in unit of years. **c** The *blue line* is the sum of IMFs 5 and 6 shown in **a**. The *orange shade* is the Multivariate El Niño/Southern oscillation Index (MEI)

IMFs 5 and 6 of Channel 6 T_B likely characterize the interannual variability related to ENSO.

For Channel 9 (Fig. 3), IMF 1 is not purely noise. Although the data have been averaged monthly, SSW in Antarctic winter 2002 (Allen et al. 2003) and Arctic winter 2009 (Yoshida and Yamazaki 2011) can still be seen from the time series (Fig. 3a, top panel). As discussed in Methods, these highly asymmetric events have been first removed from the original time series and then added back to IMF 1 to avoid strong interference with the low-frequency modes during the EJME decomposition. A dominant peak at ~0.3 year can be seen in the spectra of IMF 1. (This peak persistently exists for Channels 9–14.) IMF 2 is dominated by the SAO; however, the large ensemble deviation indicates that the SAO is weak and is comparable to noise at that level. IMF 3 is the annual cycle that dominates the T_B variations in the tropopause. IMF 4 is the near-annual variation and IMF 5 is the QBO. IMF 6 is small compared to other modes and the last IMF shows a significant warming trend of 0.5 ± 0.2 K/decade during 2002–2011. Channel 10 is sensitive to the stratospheric variability at 50 hPa. The IMFs corresponding to Channel 10 (Fig. S4) are very similar to those acquired by Channel 9.

Channels 11–14 are most sensitive to the upper stratospheric variability at 25, 10, 4, and 2.5 hPa. Eight IMFs are obtained from their T_B measurements, which are very similar (Figs. S5–S7; Fig. 4). Take Channel 14 as an example. The T_B time series acquired by Channel 14 is dominated by an asymmetric SAO (Fig. 4a, top panel). For this channel, IMF 1 is characterized by SSWs, which appear as wiggles in the monthly-averaged time series (Fig. 4b). IMF 2 is contaminated by SSWs and it has a dominant peak at ~0.3 year in its FFT spectrum. IMF 3 is dominated by the SAO. IMFs 4–6 are the annual cycle (period = 1 year), QBO-annual beats (QBO-AB; period ≈ 20 months or 1.7 years) and QBO (QBO; period ≈ 28 months or 2.3 years), respectively. IMF 7 characterizes an interannual variability (period ≈ 3 years). The last IMF shows a cooling of −0.9 ± 0.3 K during

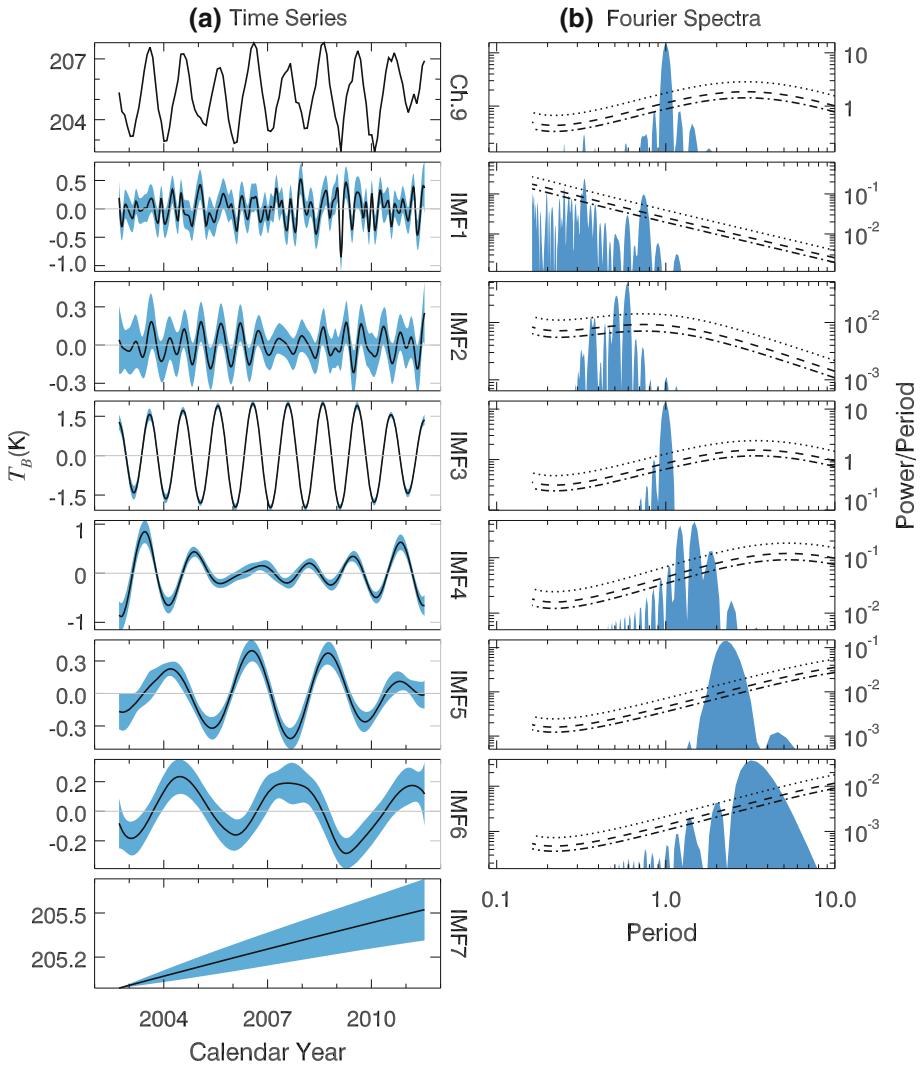

Fig. 3 Same as Fig. 2a, b except for Channel 9

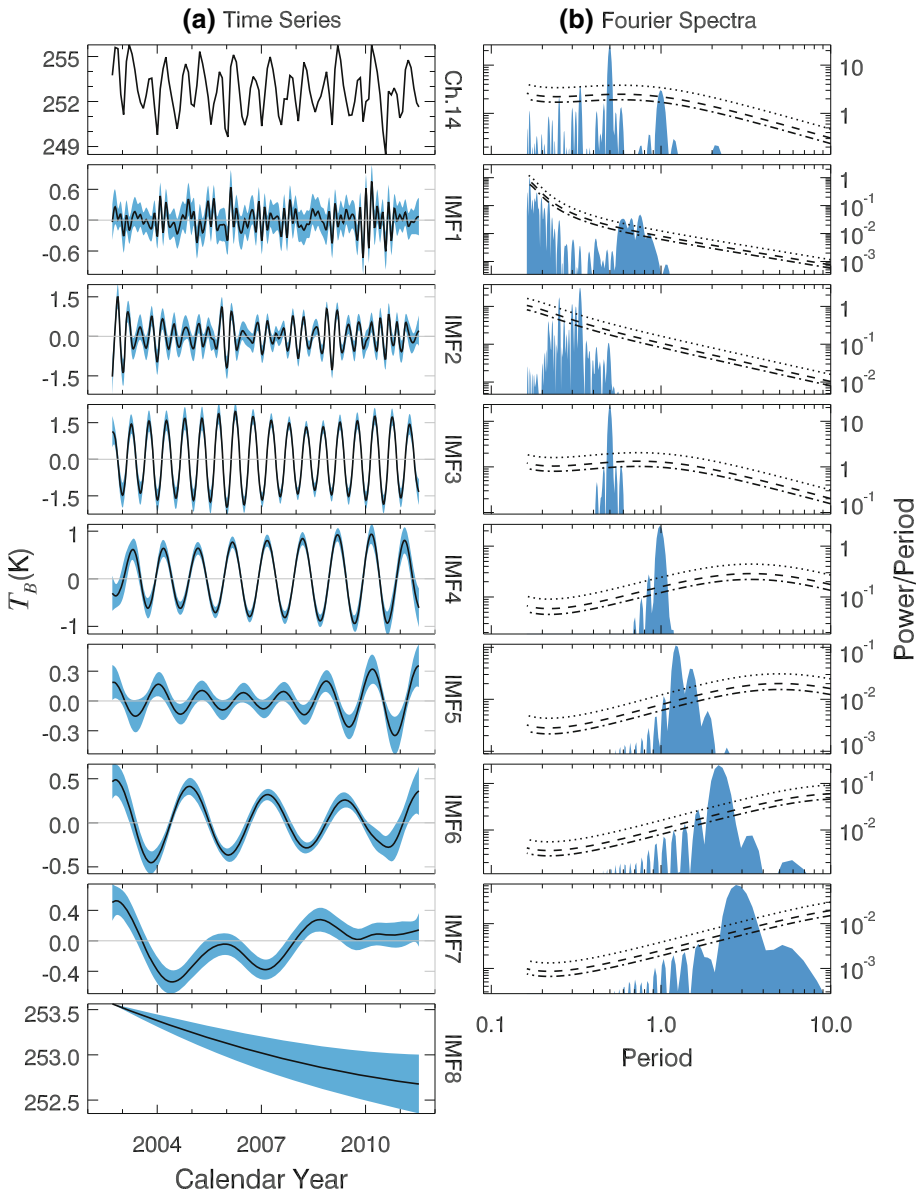

Fig. 4 Same as Fig. 2a, b except for Channel 14

2002–2011, to which the solar cycle may have partially contributed.

5 Discussions

In the previous section, the temperature time series acquired by the ten channels of AMSU-A/Aqua have been decomposed into IMFs using EJME. Their climatology and their significance to climate studies will be discussed in this section.

The decomposed IMFs can be combined to give the vertical structures of individual variability. For example, the vertical structures of the IMF amplitudes provide important information where the signal may have been originated from and amplified/damped; the vertical structures of the IMF phase differences may reveal the propagation of the signal.

5.1 The annual cycle

Figure 5a shows the time–height pattern of the extracted annual cycles from Channels 5–14 of AMSU-A/Aqua at approximate pressure levels. The annual cycle is one of the most natural variabilities in Earth's atmosphere, which is a response to the Earth's non-zero obliquity while it is orbiting around the Sun once a year; the annual cycles deviate only slightly from a perfect harmonic due to dynamical influences (Sela and Wiin-Nielsen 1971).

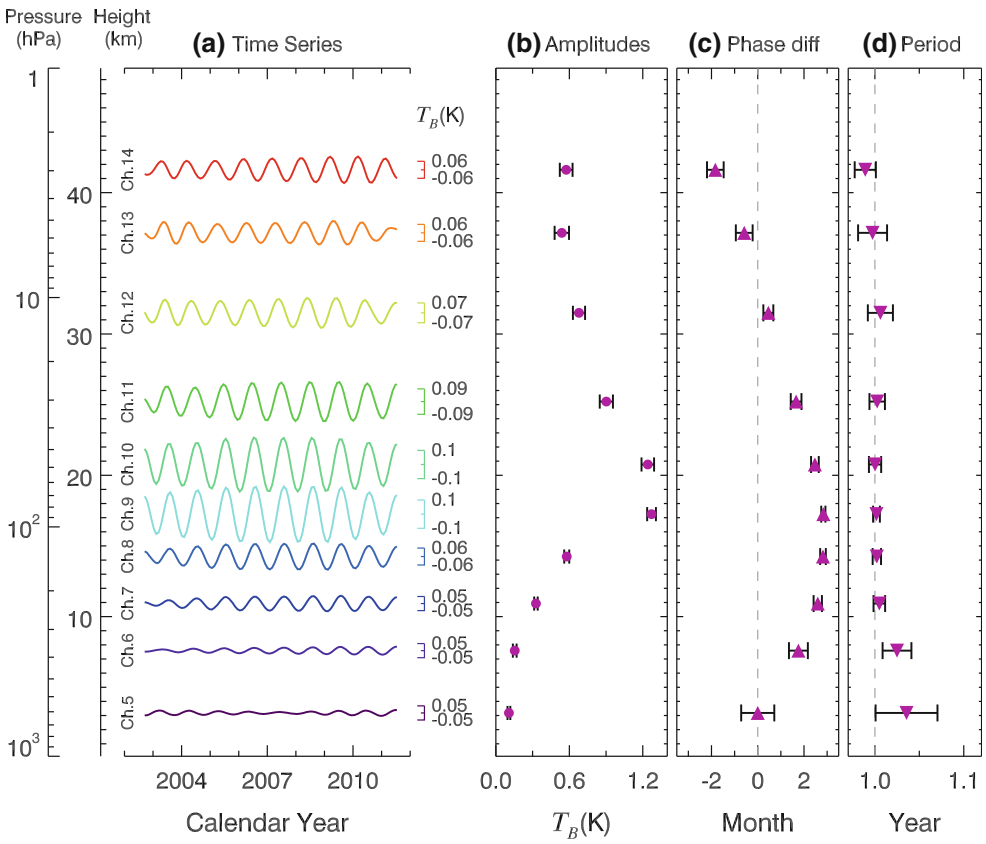

Fig. 5 **a** The ensemble means of the annual cycles extracted from the T_B data acquired from Channels 5–14. The time series are plotted at their approximated pressure levels. **b** The corresponding amplitude profiles. The *dots* are ensemble means and the *horizontal bars* are 1-σ ensemble deviations. **c** The corresponding phase profiles. The *triangles* are ensemble mean phases determined from local maxima of the filtered time series; see "Appendix 3". The *horizontal bars* are 1-σ ensemble deviations. The phases are defined relative to that at 700 hPa (Channel 5). **d** The averaged period; see "Appendix 3"

The amplitudes of the exacted annual cycles are displayed in Fig. 5b. The dot represents the ensemble mean of EJME and the horizontal bar is 1-σ ensemble deviation. The amplitude profile shows a peak of 1.3 K at the tropopause (50–100 hPa) and the amplitude drops to 0.1 K in the lower troposphere and 0.5 K in the upper troposphere. The relatively large annual cycle near the tropopause has long been noticed (Kerr-Munslow and Norton 2006; Reed and Vlcek 1969). In the tropical tropopause, the T_B annual cycle is driven by the annual variation in the upwelling branch of the Brewer–Dobson circulation and by the consequent dynamic cooling at the tropopause (Kerr-Munslow and Norton 2006; Norton 2006; Taguchi 2009). Since the upwelling becomes much weaker immediately above the tropopause (Randel et al. 2008), the amplitude of the annual cycle decreases with altitude in the stratosphere. It is also possible that the annual and SAO move the tropopause up and down considerably, thereby causing the maximum changes there.

The relative phase profile is shown in Fig. 5c. The triangles are the relative phases determined by the local maxima of the time series ("Appendix 3"), which are statistical consistent with those determined by the local minima within the error bars (not shown). A modulo of 1 year has been applied such that the phase at 700 hPa (Channel 5) is zero. This phase profile bears an intuitive explanation. Having larger heat capacity, the surface lags behind the stratosphere in response to solar forcing, and since energy is transported to the tropopause from the surface and the stratosphere, the annual cycle near the tropopause lags behind both of them.

5.2 The semi-annual oscillation (SAO)

Figure 6 shows the extracted SAO modes and the associated amplitude and phase profiles. The SAO in stratosphere and mesosphere, first discovered in 1960s, is a consequence of a series of complicated wave forcings. The detailed mechanism for equatorial SAO involves the wave–zonal flow interaction with alternating accelerations of the easterly flow by planetary Rossby waves and the westerly flow by Kelvin waves (Hirota 1980), as well as contributions from eddy forcing and the propagating gravity waves (Jackson and Gray 1994).

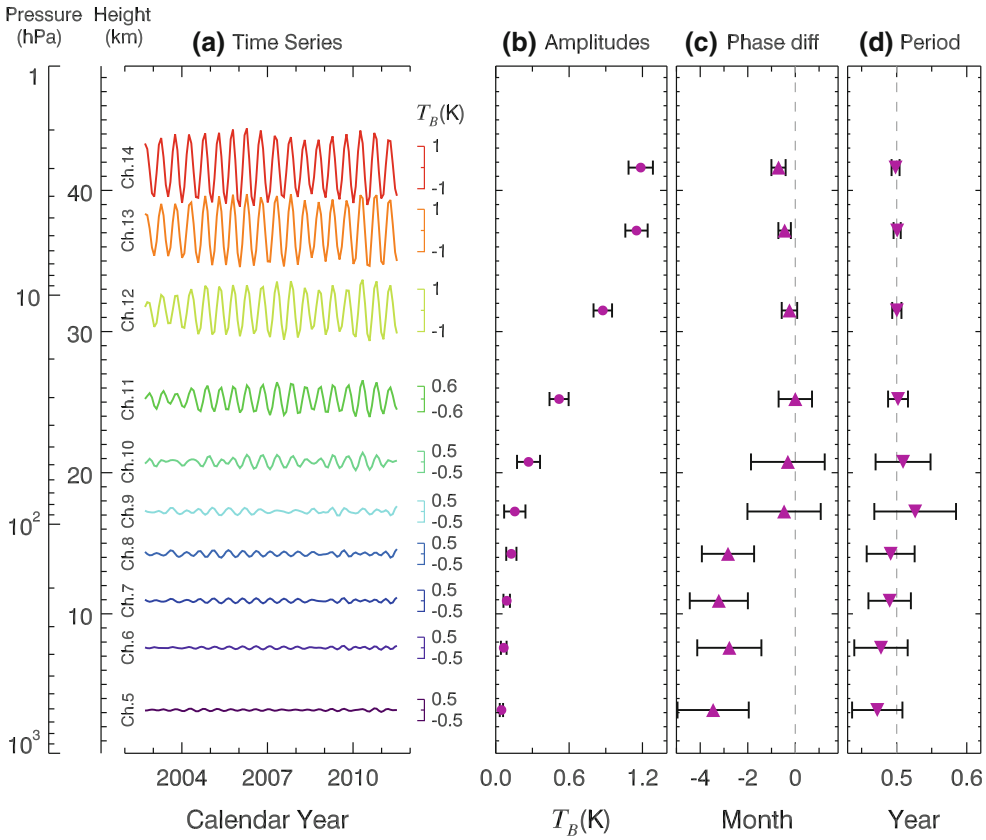

Fig. 6 Same as Fig. 5 except for the semi-annual mode and that the phases are defined relative to that at 25 hPa (Channel 11)

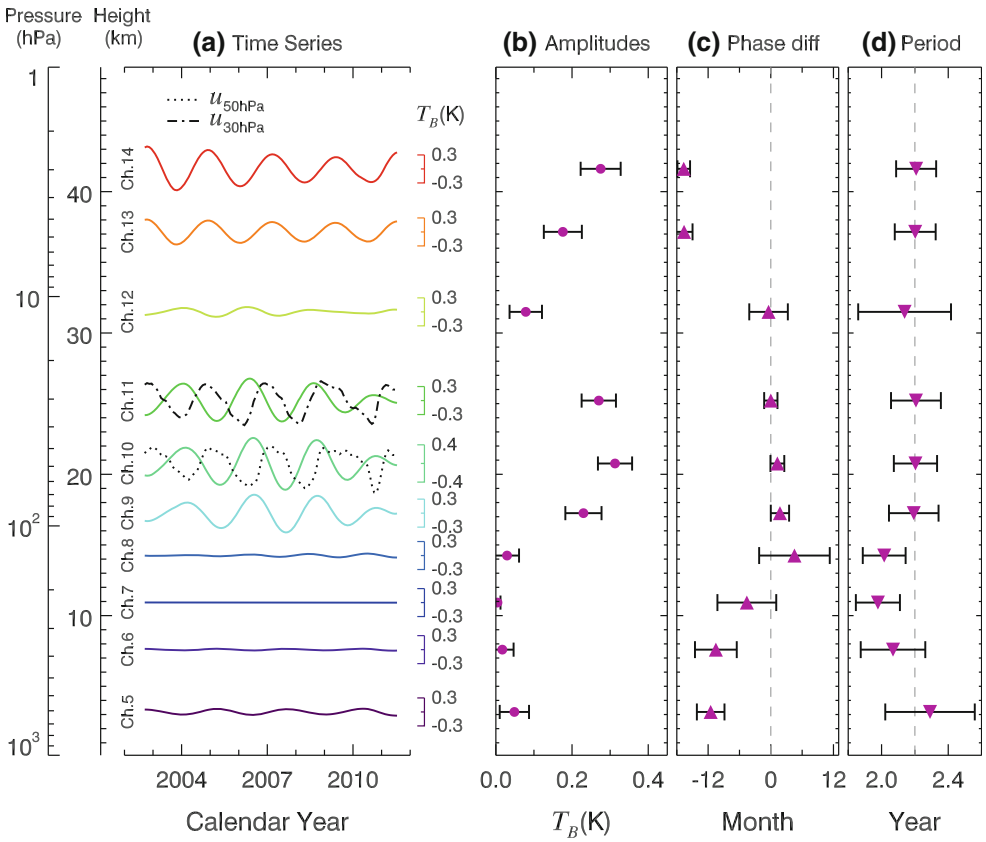

Fig. 7 Same as Fig. 5 except for the QBO modes and that the phases are defined relative to that at 25 hPa (Channel 11)

As can be seen from Fig. 6b, the amplitude of the SAO is negligibly small in the troposphere and grows quite large in the middle of the stratosphere. Because the SAO in the troposphere are not well established, the relative phases in the troposphere may not be robust and will not be discussed. A modulo of 0.5 year has been applied and the phase of Channel 11 is defined to be zero. From the phase profile, the SAO appears to be propagating slightly downward, which agrees with the observations made by Huang et al. (2006).

5.3 The QBO

Figure 7a shows evolution of the IMFs related to the stratospheric QBO. In the stratosphere, the QBO is the most dominant inter-annual variability, which is characterized by alternating downward-propagating easterly and westerly winds, driven by propagating waves confined to the equatorial regions. Although the QBO is mainly tropical, it affects the whole stratosphere and even the surface in both dynamics and chemical constitution (Baldwin et al. 2001).

It is worth noting that the extracted QBO from the AMUS-A/Aqua T_B above and below 10 hPa behaves quite differently. The amplitude of IMFs reaches minimum and has a sudden phase jump at $\sim$10 hPa (Fig. 7b, c). Using the data acquired by the Sounding of the Atmosphere using Broadband Emission Radiometry (SABER), Huang et al. (2006) found that the amplitude of QBO in temperature had two maxima in the stratosphere at 28 and 37 km and had a phase jump at 33 km during 2002–2004; meanwhile, using data acquired by the Microwave Limb Sounder (MLS) aboard the Upper Atmosphere Research Satellite (UARS), they found that the amplitude of QBO in temperature had two peaks at 4.5 and 48 hPa and a phase jump at 9 hPa during 1992–1994. These results qualitatively agree with ours.

In Fig. 7a, we overlay the standardized zonal wind anomalies at 30 hPa ($u_{30\text{hPa}}$) and 50 hPa ($u_{50\text{hPa}}$) (Naujokat 1986). The QBO modulations of AMSU-A/Aqua T_B at 30 and 50 hPa lag behind those of $u_{30\text{hPa}}$ and $u_{50\text{hPa}}$ by 3 and 5 months, respectively. This lag relation is also apparent in a ground-based measurement in the tropics, from which Kumar et al. (2011) showed that the QBO modulations in winds and temperature are almost 90° out of phase in the stratosphere and are of different downward propagation rates, as well as amplitudes and phases.

5.4 Long-term variations

The last IMFs characterize the long-term variations of T_B during 2002–2011. We derive the T_B trends by fitting a straight line to the last IMFs; the slope of the fitted line is taken as the trend. This fitting is done for every member of the ensemble calculation during EJME. The ensemble mean of the fitted slopes are shown as a blue triangle in Fig. 8, with the error bar representing the 1-σ ensemble deviation. Note that these long-term variations may not necessarily be the multi-decadal trends that are related to the anthropogenic emission of CO_2. On time-scales shorter than a decade, the Pacific decadal oscillation, the Atlantic multi-decadal oscillation, the 11-year solar cycle, ENSO, and sporadic volcanic aerosol emissions may all contribute.

There is a cooling trend of -1 ± 0.4 K/decade at 2.5 hPa in the upper stratosphere, which drops to zero at 25 hPa. The cooling trend in the upper stratosphere is consistent with previous studies (Randel et al. 2009; Santer et al. 2003). The trend becomes positive in the upper troposphere and attains a maximum of 1 K/decade at 90 hPa in the tropopause, which seems to contradict with previous findings, which suggest a cooling trend (-0.5 K/decade) in the tropopause (Seidel et al. 2001). Lastly, there are cooling trends of -0.1 ± 0.1 K/decade (c.f. Sect. 4.2) and -0.25 ± 0.15 K/decade are observed at 700 and 500 hPa, respectively.

To test the robustness of the extracted trends, we perform another line fitting using the deseasonalized raw data (orange dotted line in Fig. 8). These trends are consistent with those extracted by EJME. In addition, we further examine the uncertainty due to the finiteness of the time series by repeating the line fitting for September 2003–August 2010 only. The results are shown as the red dash-dotted line in Fig. 8. The trends in the troposphere obtained using the shortened data becomes slightly positive (<0.1 K/decade). The trends remain positive and negative in the tropopause and the stratosphere. The negative trends in the middle stratosphere between 2.5 and 25 hPa seems to be more robust but is weaker than that obtained using the

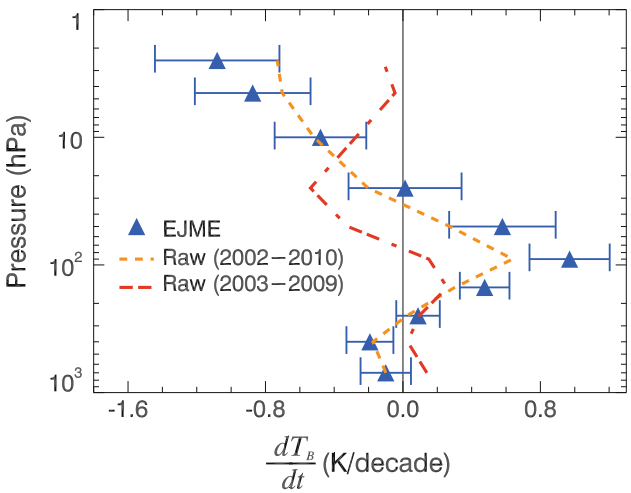

Fig. 8 Nine-year trends for Channels 5–14. The *blue triangles* are EJME ensemble means. The *horizontal bars* are 1-σ ensemble deviations. The *orange dot line* and *red dash-dotted lines* are linear trends of deseasonalized raw data

longer data. These results suggest that the trends are highly dependent on the time range. In particular the trends in and below the tropopause may not be significant due to the aforementioned decadal variability in the atmosphere and the ocean (Thorne et al. 2011).

The stratospheric trends we found from the AMSU-A/Aqua data are more robust. There have been discussions on the cooling trends observed in the stratosphere. Randel et al. (2009) used the multi-variate linear analysis to show a cooling of −0.5 K/decade in the lower stratosphere using radiosonde and satellite data between 1979 and 2007, and a cooling between −0.5 and −1.5 K/decade in the middle and upper stratosphere using Stratospheric Sounding Unit (SSU) data between 1979 and 2005. These values are consistent with our values derived from EJME and the raw fitting using data for September 2002–August 2010. Part of the cooling trend in the stratosphere may be due to an increase in the tropopause height (Santer et al. 2003).

5.5 Stratospheric QBO-AB and tropospheric near-annual variability

The near-annual variability exists in both troposphere and stratosphere, which are imprinted in the third-last IMF of the time series of all channels and are shown in Fig. 9a. Figure 9b shows that the amplitudes reach maximum around the tropopause, which is similar to that of the annual mode. The phase profile is shown in Fig. 9c, which shows that while there are little phase differences between the time series within the stratosphere and the troposphere, there is a 6-month lag of the stratospheric data with respect to the tropospheric data.

The stratospheric near-annual variability is likely due to the QBO-AB, which was first reported by Baldwin and Tung (1994) and is the most pronounced QBO-related harmonics. It has periods of ∼20 and ∼8.6 months (Tung and Yang 1994) and is believed to be produced from the non-linear interaction between QBO and annual mode (Jiang et al. 2005).

The tropospheric near-annual mode appears as a new variability that has not been previously reported. Here we present another evidence of the near-annual variability in the assimilated air temperature. In Fig. 9a, we overlaid the time–altitude pattern of NCEP air temperature data, which have been filtered by a Fourier band-pass filter with the band window set between 14 and 22 months and have been averaged longitudinally between 5°S–5°N and 160°E–270°E. Note that the NCEP data do not extend beyond

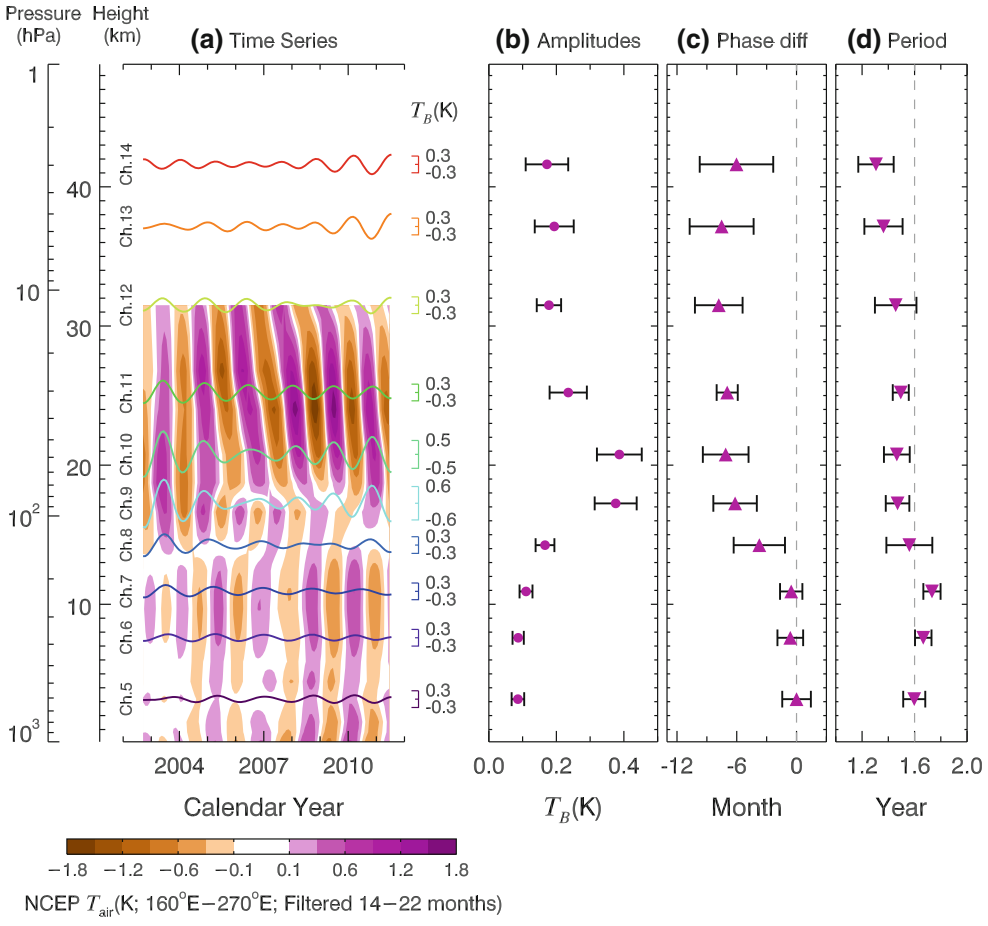

Fig. 9 Same as Fig. 5 except for the near-annual cycles. The phases are defined relative to that at 700 hPa (Channel 5). In **a**, NCEP air temperature data averaged between 5°S and 5°N and zonally between 160°E and 270°E are overlaid. The NCEP data have been filtered by the Fourier band-pass filter for 14–22 months

10 hPa. The positions of maxima and minima of the NCEP data match with those of the time series quite well. The spatial patterns of the NCEP data also reveal that the near-annual modes in the troposphere and the stratosphere (i.e. QBO-AB) behave differently and are separated by the tropopause at ~100 hPa. While QBO-AB propagates downward, the near-annual mode in the troposphere appears to propagate slightly upward and is much weaker. The amplitude of the near-annual signal in the troposphere reaches a maximum at about 300 hPa and quickly diminishes above 200 hPa.

The tropospheric near-annual mode may be related to a near-annual mode in the ocean. Jin et al. (2003) found a near-annual mode in the central eastern Pacific Ocean by applying a 22-month high-pass filter and the wavelet analysis to the NCEP assimilated SST during 1990–2001. Their later work (Kang et al. 2004) reproduced similar results by removing the climatological annual cycle and the local linear trend in SST, zonal wind, zonal current, and sea level height during the period of late 1998 through the end of 2001. This same mode, referred to as sub-ENSO by Keenlyside et al. (2007), was also identified during 1990 and 2004 by Multichannel Singular Spectrum Analysis. Using a harmonic extraction scheme, the near-annual mode was also observed from 1985 to 2003 by Chen and Li (2008) as a mode well separated from ENSO.

Interestingly, none of these works mentioned the better-known tropospheric biennial oscillation (TBO) in the SST and surface wind, which has a period of ~2 years. TBO was first discovered in the south Asia and Indian monsoon and may interact broadly with other tropical and extra-tropical processes (Tomita and Yasunari 1996). It is thought to be local in the tropical Pacific and Indian Ocean regions and has a tendency to alternate between strong and weak years (Pillai and Mohankumar 2010). In fact, the spectral analysis of SST and surface wind by Rasmusson and Carpenter (1982) of the eastern Pacific showed peaks at ~24 months for 1953–1974 data. This TBO was further studied by Meehl (1987) using Indian monsoon rainfall as a long-term index. Meehl observed that this signal was not strictly biennial and that it was accompanied by anomalies in the westerly wind in the western Pacific, which were then followed by anomalies in the SST in eastern Pacific. In the subsequent studies, Meehl and his collaborators (Meehl 1993, 1997; Meehl and Arblaster 2011; Meehl et al. 2003) proposed mechanisms involving coupled land–atmosphere ocean processes over a large area of the Indo–Pacific region. It is still not clear whether the near-annual mode observed during recent decades and the biennial mode observed in earlier decades are in fact the same mode with changed period. It is not even clear, having so few data, whether the TBO reported before was indeed biennial. Nonetheless, whatever it may be, the near-annual mode in the ocean, which has amplitude ≥1 K (Jin et al. 2003), will inevitably propagate into the atmosphere.

To demonstrate the coherence between the near-annual mode in the ocean and the near-annual mode in the atmosphere, we present in Fig. 10 the Hovmöller diagrams of the near-annual variability in NCEP surface air temperature at 1,000 hPa (colour contours) and the observed SST from TRMM. The data have been filtered by the same Fourier band-pass for 14–22 months and have been averaged between 5°S and 5°N. The near-annual signal in the NCEP surface air temperature is most pronounced in the eastern Pacific region and appears to be propagating westward. Maxima and minima of the SST pattern

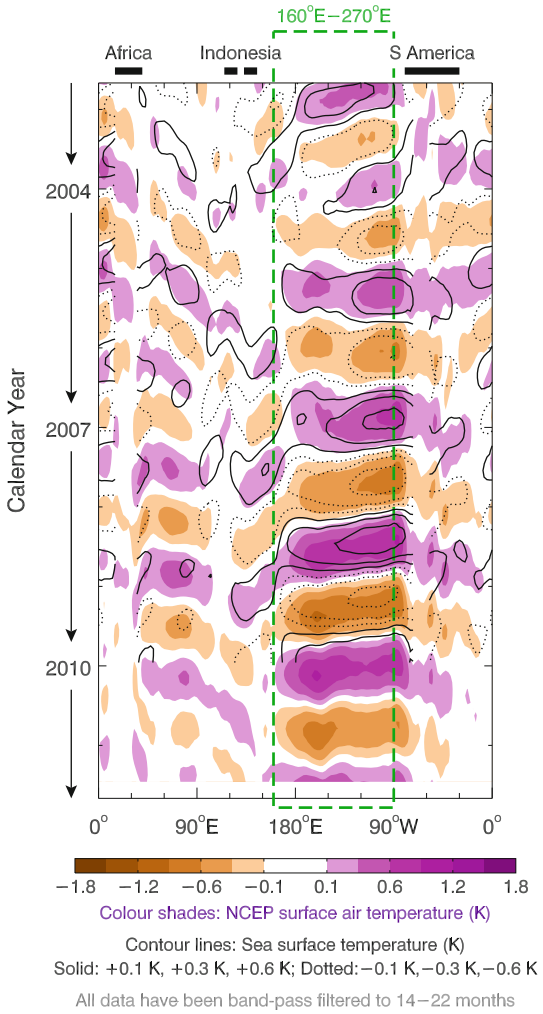

Fig. 10 Hovmöller diagrams of the near-annual variability in NCEP-1 surface air temperature at 1,000 hPa (*colour shades*) and sea surface temperature (SST) before December 2009 observed by the Tropical Rainfall Measuring Mission's (TRMM) Microwave Imager (TMI; *black contour lines*) All data have been band-pass filtered for 14–22 months and averaged between 5°S and 5°N. The *green box* encloses the longitude bands where the near annual variability is the strongest. Notice the absence of the SST data over the continents

synchronize with those of the air temperature pattern. The amplitude of the near-annual mode in the ocean is also coherent with that of the near-annual mode in the atmosphere.

6 Conclusions

Nine years of atmospheric brightness temperature of unprecedented quality acquired from AMSU-A are used for studying climate change. We have presented a detailed description of the variability and the long-term variations imprinted in the AMSU data. These variabilities have been extracted using the non-linear, adaptive method called the Ensemble Joint Multiple Extraction (EJME), which is empirical and does not require any prior knowledge of the system.

EJME combines the advantages of DMP and EEMD. The former can effectively avoid scale mixing while the latter has less end-point effects for finite time series. Before applying EJME to the AMSU temperature data, strong and highly asymmetric events in the time series related to SSW were first removed. With this preprocessing, we show that EJME can successfully extract the known atmospheric variabilities, including SAO, annual cycle, near-annual mode, QBO, QBO-AB and ENSO. Using ensembles of decompositions, the statistical stability of EJME has been demonstrated.

The amplitudes and the phase relationships of the extracted modes as functions of altitudes from the lower troposphere to the upper stratosphere have been examined. The amplitude of the SAO decreases with decreasing altitude. This is consistent with the stratospheric origin of SAO. The annual mode has a peak amplitude of $\sim$1 K at the tropopause, which may be a combined effect of the dynamical cooling due to the upwelling below and the annual variations of the tropopause height. The QBO mode has a bimodal amplitude structure, having a minimum of $\sim$0.1 K at 10 hPa and maxima of $\sim$0.3 K at 2 and 50 hPa, which agrees with previous studies. The ENSO mode is the strongest at 700 hPa, showing an amplitude of $\sim$0.3 K and good correlation with the MEI index lagged by 0.24 year.

The long-term variations of the temperature show a significant cooling trend in the upper stratosphere during 2002–2011; it ranges from $-$0.4 K at 10 hPa to $-$0.8 K at 1 hPa during the 9-year observational period. The trend shows some warming near the tropopause and slightly negative in the troposphere, but these trends are not statistically significant.

EJME is also capable of extracting a new tropospheric near-annual mode. The near-annual mode has peak amplitude of 0.4 K at the tropopause; its amplitudes are relatively small at other altitudes, 0.1 and 0.2 K in the troposphere and the stratosphere, respectively. While the near-annual mode in the stratosphere is likely to be a manifestation of the QBO-AB, its origin in the troposphere is not clear, although previous studies also found similar near-annual variability in the SST and zonal wind. We have confirmed its existence in the troposphere from the NCEP air temperature data using a simple FFT filter that captures signals with periods between 14 and 22 months.

The AMSU data are an example of what we could learn from a high quality dataset. While more detailed analyses of AMSU data, including spatial distributions of modes and trend, are awaiting, it is already a challenge for climate models to simulate the tropically averaged principal modes of natural variability and trends, the success of which would raise our level of confidence in climate models (Forest et al. 2002; Huang et al. 2011).

Acknowledgments We thank Dr. Dong L. Wu for critical comments and two anonymous referees for constructive criticisms that improved this paper. YS was supported by Overseas Research Fellowship of the Faculty of Science and Department of Physics, The University of Hong Kong. The extraction of the AMSU-A/Aqua data from the Atmospheric InfraRed Spectrometer (AIRS)/AMSU-A data archive was supported by a research grant administered by Dr. Ramesh Kakar, EOS Aqua Programme Scientist at NASA Headquarter and the Keck Institute for Space Studies at California Institute of Technology. We also thank Dr. Thomas Hearty for proofreading our paper and sharing his results on AIRS data. The TMI SST data were downloaded from ftp://ssmi.com/tmi/. The standardized zonal winds at 30 and 50 hPa ($u_{30\text{hPa}}$ and $u_{50\text{hPa}}$) were downloaded from http://www.cpc.ncep.noaa.gov/data/indices/. The MEI index for ENSO was downloaded from http://www.esrl.noaa.gov/psd/enso/mei/. YLY designed the approach; HHA provided the monthly-averaged AMSU-A/Aqua data; TYH and ZS provided the DMP package; ZS and YS developed the EJME package; YS performed the time series decomposition; KFL, YLY, and YS interpreted the results and wrote most of the manuscript.

Appendix 1: Random re-sampling of AMSU-A/aqua observations

Each day the Atmospheric InfraRed Sounder (AIRS) aboard Aqua generates $\sim$3 million spectra, which are stored in 240 files totaling $\sim$20 GBytes of calibrated radiances each day. Spatially co-located with the AIRS spectra are the brightness temperatures from 15 AMSU channels, which add another $\sim$120 MB. In order to reduce this data volume for operational calibration, $\sim$3,400 sample measurements from daytime (1:30 p.m.) orbits and another 3,400 sample measurements from night-time (1:30 a.m.) orbits have been randomly selected and are stored in the AIRS Calibration Subset Product (AIRXBCAL), which can be downloaded from http://disc.sci.gsfc.nasa.gov/AIRS/data-holdings. The primary objective of the Calibration Subset Product is to aid in verifying the calibration of AIRS, AMSU and visible channel radiances relative to truth on the Earth's surface.

However, a part of the AIRXBCAL data save randomly selected near-nadir (defined below) samples. It is this random subset of AMSU-A/Aqua footprints collected in the AIRXBCAL products which is used in this study.

The re-sampling of AMSU-A/Aqua radiances are based on a random re-sampling algorithm for AIRS spectra. The AIRS and AMSU-A/Aqua data from each day are grouped in 32,400 cross-track scan line. The AIRS and AMSU-A/Aqua scan lines have 90 and 30 footprints, respectively, both covering ±49° from nadir (downward vertical line from the satellite). Therefore, the cross-track resolution of AIRS is 3 times finer than that of AMSU-A/Aqua. For AIRS, 6 of the 90 footprints are located at ±0.55°, ±1.65°, and ±2.75° from nadir; the measured spectra of these 6 footprints are referred to as the "near-nadir" spectra. Each day, there are 194,400 (=32,400 × 6) near-nadir AIRS spectra, from which ~18,000 spectra are randomly selected as follows: Each scan line has an associated satellite latitude θ. Let $\rho = [0,1]$ be a uniformly-distributed random number. If $\rho/\cos\theta \leq 0.14$, one of the 6 near-nadir AIRS footprints is randomly selected from that scan line. The $\rho/\cos\theta$ term removes the spatial over-sampling characteristic of polar orbiting satellites. This is important for climate application using global averages, so that 50 % of the randomly re-sampled near-nadir spectra correspond to the area between 30°S and 30°N, as expected by integrating over the sphere. Finally, for a selected AIRS footprint that lies within +0.55° and +2.75° of nadir, the corresponding AMSU-A/Aqua footprint at +1.65° will be taken, of which the measured radiance will be used for operational purposes such as determination of the presence of clouds. Similarly, for a selected AIRS footprint that lies within −0.55° and −2.75° of nadir, the corresponding AMSU-A/Aqua footprint at −1.65° will be taken.

Figure 11a shows the spatial coverage of 17,594 re-sampled near-nadir AIRS footprints on 7 Janurary, 2007. Note the thinning of the re-sampling density near the polar regions. To further illustration the random re-sampling, Fig. 11b shows a zoom-in of an Aqua swath near Hawaii on the same day. For comparison, the full field-of-views (FOV) of both AIRS and AMSU-A/Aqua span over ±49° from nadir, which is shown as green in the figure. For the AIRXCAL product, only AIRS footprints within ±3.3° from nadir (shown as orange) are randomly selected. For

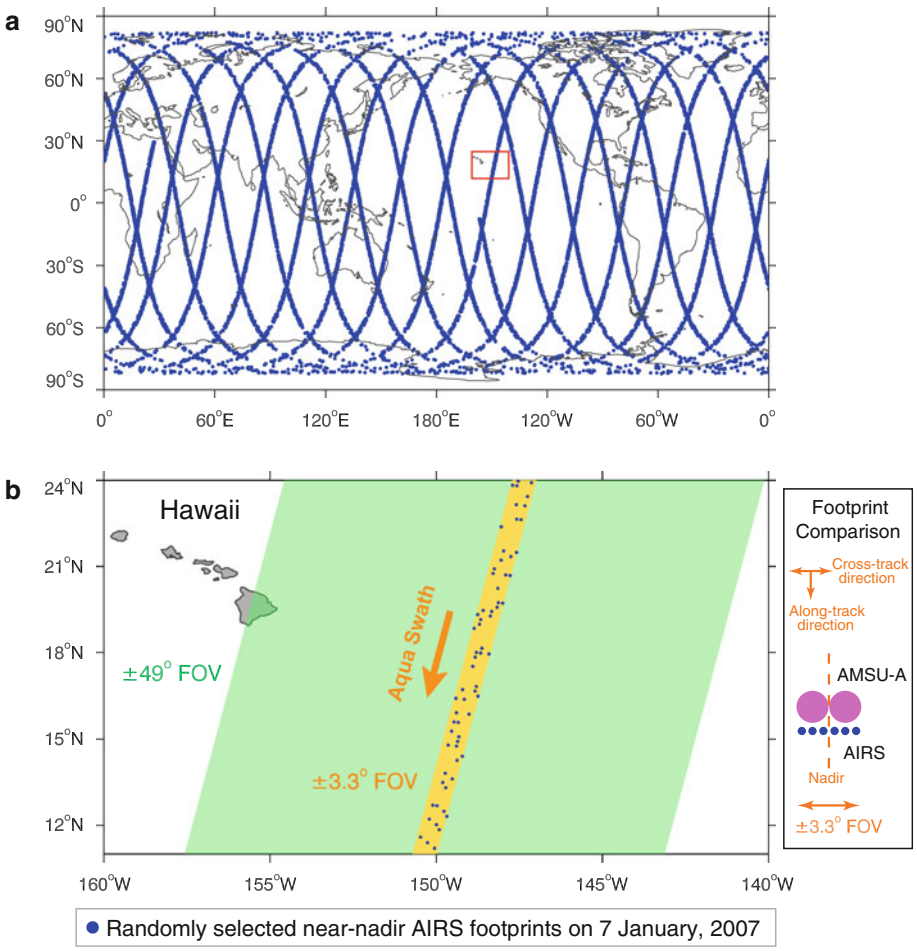

Fig. 11 **a** The spatial distribution of randomly selected AIRS footprints within ± 3.3° from nadir (i.e. near-nadir observations) on January 7, 2007. The random selection is performed in the way that more footprints closer to the equator are selected such that 50 % of the total selected footprints come from the area between 30°N and 30°S. Note the thinning of density of the selected footprints near the poles; **b** A zoom-in of a descending Aqua swath near Hawaii. The *blue dots* representing the randomly selected AIRS footprints are the same as those shown in **a**. Both AIRS and AMSU-A/Aqua have a full field-of-view (FOV) of ± 49° from nadir (*green*). Only footprints within ± 3.3° from nadir (*orange*) are randomly selected for calibration purposes, which are stored in the AIRXCAL product

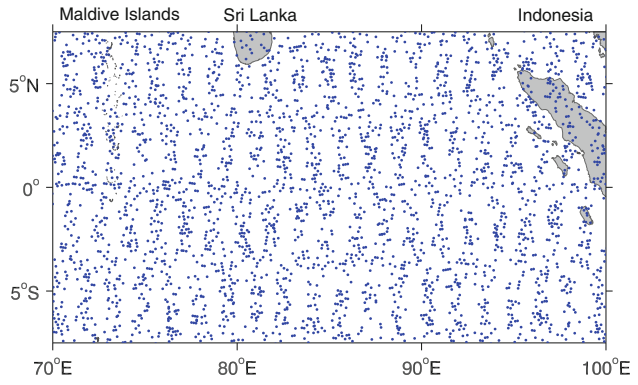

Fig. 12 The spatial coverage of the re-sampled AIRS footprints between 1 January, 2007 and 16 January, 2007 over the equatorial Indian Ocean. The major islands are labeled

each cross-track scan line, none or more than one of the AIRS footprints may be selected. The AMSU-A/Aqua footprint (either at +1.65° or −1.65° from nadir) closest to the selected AIRS footprint is taken, as illustrated on the right of Fig. 11b.

Same as the original data, the re-sampled orbit will repeat in exactly 16 days. An example of the spatial coverage of the re-sampled data points over the equatorial Indian Ocean is shown in Fig. 12. This time period included 232 orbits, but data 3.5 orbits are missing, seen as the thinner spatial coverage, due to various spacecraft maneuvers.

Appendix 2: Ensemble joint multiple extraction (EJME)

Mathematical formulation

To state the data analysis method in a clearer manner, let $X(t_i)$, $i = 1,2,\ldots,N$, be a time series. We replace data points during SSW with moving monthly average. The time series is then decomposed by $X(t_i) = X^{(0)}(t_i) + S(t_i)$, where $X^{(0)}(t)$ is the masked data and $S(t)$ is SSW events. The most prominent peaks in the Fourier spectrum of $X^{(0)}(t)$ are identified, and the initial guess of the phase function $\theta_k^0(t)$ for DMP is estimated. Using DMP, $X^{(0)}(t)$ is decomposed into m modes $g_k^{(0)}(t)$ and residual $R^{(0)}(t)$ as:

$$X^{(0)}(t_i) = \sum_{k=1}^{m} g_k^{(0)}(t_i) + R^{(0)}(t_i).$$

In our analysis, we identify characteristic time scales from the spectra of the time series. For tropospheric data, four initial guesses of $\theta_k^0(t)$ are used corresponding to harmonics with periods of 0.5, 1.0, 1.6 and 2.2 years. For stratospheric data, five initial guesses of $\theta_k^0(t)$ are used corresponding to harmonics with periods of 0.3, 0.5, 1.0, 1.6, and 2.2 years. In DMP iterations, if the retrieved period drifts away from the initial guess, the initial guess will be slightly perturbed and the DMP iterations will be repeated.

Due to the end point problem of DMP, the residual $R^{(0)}(t)$ may still contain signals at both ends of the time series. To resolve the end issue, EEMD is employed to pick up signals from the ends. Using EEMD, $R^{(0)}(t)$ is decomposed by

$$R^{(0)}(t_i) = \sum_{j=1}^{n} c_j^{(0)}(t_i) + r^{(0)}(t_i)$$

where $c_j^{(0)}(t)$ are IMFs and $r^{(0)}(t)$ is the EEMD residual. In our analysis, the noise used in EEMD is 0.2 of the standard deviation of the time series and the ensemble number used is 150. The ensemble number may seem to be small, but taking into account that this process will typically be repeated more than ten times, the total ensemble number is considerable.

Whenever the spectral correlation of $c_j^{(0)}(t)$ and $g_k^{(0)}(t)$ is larger than 0.5, $c_j^{(0)}(t)$ is masked by a plateau-like weighting function $W(t)$ and combined with $g_k^{(0)}(t)$ to become the k-th mode

$$f_k^{(0)}(t_i) = g_k^{(0)}(t_i) + W(t_i)c_j^{(0)}(t_i)$$

where $W(t)$ is chosen as

$$W(t) = \theta(t_a - t) + (1 - \theta(t_a - t))e^{-\alpha(t_a - t)^2} + \theta(t - t_b) + (1 - \theta(t - t_b))e^{-\alpha(t - t_b)^2}$$

Here (t) is the Heaviside step function and t_a, t_b and α are some constants. In our analysis we choose $t_a = 2003.25$, $t_b = 2011.25$ and $\alpha = 2$. After recombination, the residual

$$X^{(1)}(t_i) = X^{(0)}(t_i) - \sum_{k=1}^{m} f_k^{(0)}(t_i)$$

is used in place of $X^{(0)}(t)$ as the time series for the next round of extraction.

Let $\varepsilon > 0$ be some preset small amplitude. The iteration is terminated at the p-th cycle if for all $k = 1, 2, \ldots, m$, the standard deviation of $\left\{f_k^{(p)}(t_i), i = 1, 2, \cdots, N\right\}$ is smaller than ε. In our analysis, ε is chosen to be 0.1 % of the standard deviation of $X^{(0)}(t)$.

The k-th mode of the original data is defined as the summation of all the k-th extracted mode from each round of extraction:

$$f_{0,k}(t_i) = \sum_{j=0}^{p-1} f_k^{(j)}(t_i)$$

And the data is now decomposed by

$$X^{(0)}(t_i) = \sum_{k=1}^{m} f_{0,k}(t_i) + X^{(p)}(t_i)$$

In our case, after such treatment, the residual $X^{(p)}(t)$ contains only very low frequency and very high frequency

components, which are readily separable by EEMD. The EEMD decomposition of $Y^{(0)}(t) = X^{(p)}(t)$ is

$$Y^{(0)}(t_i) = \sum_{k=1}^{n} L_k^{(0)}(t_i) + T^{(0)}(t_i)$$

where $L_k^{(0)}(t)$ are the IMFs and $T^{(0)}(t)$ is the residual. In our analysis, the noise used in EEMD is 0.2 of the standard deviation of the time series and the ensemble number used is 150. The anomaly mode $A^{(0)}(t)$ is obtained by summing up all the low frequency IMFs:

$$A^{(0)}(t_i) = \sum_{k=s}^{n} L_k^{(0)}(t_i)$$

In our analysis, by the length of the time series, EEMD chooses $n = 6$ and we choose $s = 5$. Since the decomposition of low frequency components is usually affected by high frequency ones, we put $Y^{(1)}(t)$ in place of $Y^{(0)}(t)$ and repeat the EEMD extraction again. Here $Y^{(1)}(t)$ is defined by

$$Y^{(1)}(t_i) = Y^{(1)}(t_i) - A^{(0)}(t_i)$$

This process is terminated at the q-th cycle if the standard deviation of $\left\{A^{(q)}(t_i), i = 1, 2, \ldots, N\right\}$ is smaller than ε. In our analysis, ε is chosen to be 0.1 % of the standard deviation of the linearly detrended Y(0)(t). The anomaly mode is obtained by

$$A_0(t_i) = \sum_{j=0}^{q} A^{(j)}(t_i)$$

Finally, the data is decomposed by.

$$X(t_i) = \sum_{k=1}^{m} f_{0,k}(t_i) + A_0(t_i) + T_0(t_i) + H_0(t_i)$$

where $T_0(t) = T^{(q)}(t)$ is taken as the trend, and the residual $H_0(t)$ is the sum of high frequency components and $S(t)$.

Since this method is far too complicated for direct analysis, we employ the noise assisted method to control its quality and test its stability. We obtain an ensemble of M decompositions by adding white noise to the data $X_i(t) = X(t) + N_j(\sigma,t)$ where $N_j(\sigma,t)$ is some white noise with standard deviation σ. The decomposition ensemble with input uncertainty σ is

$$E(\sigma,t) = \left\{ D_j(\sigma,t) = (f_{j,k}(t), A_j(t), T_j(t), H_j(t)) : X_j(t) = \sum_{k=1}^{m} f_{j,k}(t) + A_j(t) + T_j(t) + H_j(t) \right\}$$

The "true" decomposition $D(\sigma, t)$ with input uncertainty σ is taken to be the ensemble average

$$D(\sigma,t) = \frac{1}{M}\sum_{j=1}^{M} D_j(\sigma,t) = (f_k(t), A(t), T(t), H(t))$$

For each input uncertainty σ, there will be some associated uncertainty in the output. The relation between input and output uncertainty is intrinsic to the data analysis method.

End points problems in EJME

Both DMP and EEMD used in EJME have end points problems. In DMP, the end points problem arises when one periodically extends a non-periodic time series. Since FFT is used as the iterative kernel in DMP, whenever the time series is non-periodic, the infinitely extended time series will be discontinuous at the end points. With only a finite number of terms, energies near the discontinuities will not be fully captured by FFT, and hence not by DMP. Typically, the end problem of DMP is manifested by the attenuation of IMFs towards the ends. Examples can be found in Hou and Shi (2011). In EEMD, the end problem is caused mainly by cubic spline fitting, which artificially deforms features of the time series especially at the ends. This problem is more serious for low-frequency modes, which have very few numbers of maxima and minima for constructing upper and lower envelopes, resulting in unregulated wings at end points.

The end points problem in DMP leads to leakage of signals at the ends. Moreover, when IMFs are attenuated, the residual becomes significant towards the ends, and this strongly interferes with the estimation of the trend and makes the resolution of the end points problem indispensable. Although EEMD has its end points problem as well, the noise-assisted process tends to randomize the end points so that deterministic errors can usually be reduced. In practice, the end points problem of EEMD is significantly less serious than that of DMP when applied to real data. Hence in our analysis, in order to give a better estimation of trends, we employ EEMD to ameliorate the end points problem of DMP, and reduce the energy of the residual near the end points at the expense of introducing in them some possible arbitrariness. As a consequence, as can be seen in Figs. 2, 4 and 5, the 1-σ ensemble deviation is typically larger at end points than in the middle of each IMF, and yet the estimation of trend is made better, since the end points of a time series, which interfere strongly with the estimation of trend, have now been fully extracted.

Stability of EJME

Neither IMFs by EEMD nor DMP are perfect in the presence of noise. Using these two methods jointly, the

reliability of EJME needs to be assessed before any result obtained by it can be taken seriously. Since there is no unique decomposition of any given time series, what can be taken as a "true" decomposition is quite ambiguous. So instead of asking whether the decomposition is "true", it is more appropriate to ask how stable it is in response to perturbations in the input and changing of parameters in the data analysis method. Whenever a decomposition is verified to be stable, it is plausible to accept it as a reasonable decomposition of a given time series.

Since DMP is an optimization algorithm, one may think of mode decomposition as a process of searching for the "ground state" of a system, in which the iteration processes could sometimes converge to some pseudo-stable state instead of the lowest energy state. Although it is unlikely that we can ever affirm a stable state to be the ground state, we can always verify its stability by adding noise to the test, and kick the system into some lower energy states whenever they do exist in the vicinity. For any data analysis method, whenever the "thermal activation" is strong enough, the system will always "ionize" and the results will diverge. Yet for a good data analysis method, the uncertainty in the results should be constrained for a range of moderate perturbations.

Since parameters in EJME are chosen according to the features of time series, they are not totally free to change. While perturbing some parameters may be fatal to the results, changing some others has limited effects. Hence in this paper, we fix all parameters as stated in "Appendix 2.1" and investigate only the stability of mode decomposition upon perturbations in the input. We perform a Monte Carlo simulation, where an ensemble of EJME IMFs, $\{IMF(t) : EJME\{X(t) + \alpha\sigma_X\tilde{N}(t)\}\}$, is obtained by adding an artificial white noise to the raw time series $X(t)$, where $\tilde{N}(t)$ is a Gaussian noise with unit standard deviation, σ_X the standard deviation of the de-trended $X(t)$, and α a constant. Note that this is the second Monte Carlo simulation that is similar to the one employed in EEMD during EJME. The standard deviation of $\{IMF(t)\}$, denoted by σ_{IMF}(t), characterizes as the sensitivity of EJME in response to the measurement noise. For simplicity, we define the sensitivity $\bar{S}$ as the time average of σ_{IMF}(t).

Taking AMSU-A/Aqua Channel 5 as an example, $\bar{S}$ is plotted as a function of α in Fig. 13. Three tests are run for each α, and the EJME ensemble number used in the noise tests is 200. $\bar{S}$ of IMF 1, denoted by $\bar{S}(IMF1)$, is linearly growing with α, indicating that $\bar{S}(IMF1)$ is simply the artificial noise in the Monte Carlo simulation. $\bar{S}(IMF2)$ shows a transition when $\alpha \approx 7\%$, after which the dependence on α is much weaker. The same applies for other IMFs 3–7: $\bar{S}$saturates and its dependence on α is much weaker when $\alpha \geq 7\%$. This show that $\bar{S}$ saturates $\alpha \geq 7\%$.

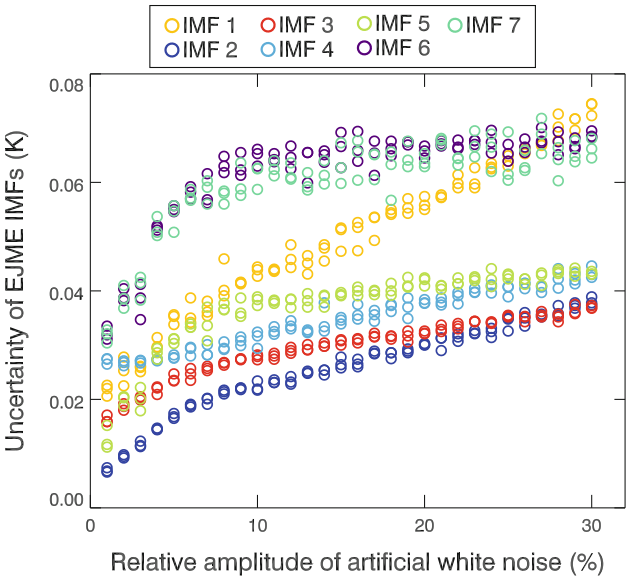

Fig. 13 Stability test for EJME using T_B of AMSU-A Channel 5 as an example. The amplitude of the artificial white noise is defined relative to the standard deviation of the linearly de-trended data. Each Monte Carlo simulation composed of 200 ensemble runs and the standard deviation of the EJME IMFs was calculated at each time coordinates; in this figure, the time-averaged uncertainty is shown so that each run is represented by *one circle*. Three different Monte Carlo simulations (all of sizes 200) were carried out

Here we have shown the noise test for monthly-averaged data of AMSU Channel 5 only, and the results for other channels are qualitatively similar. For our results presented in Sects. 4 and 5, we used one standard deviation of IMF 1 for EJME, which is $\sim 0.25\sigma_X$. That is, the perturbation we have used in our work is taken within a range where $\bar{S}$ is insensitive to α.

Appendix 3: Amplitude and phase determinations

In Sect. 4.3 we discussed the amplitude and phase of an extracted IMF using EJME. The amplitude has been defined as the standard deviation of the time series. Below we describe how the phase has been defined.

Given a time series with at least one local maximum, let $t_1^{\max}, t_2^{\max}, \ldots, t_n^{\max}$ be the time of the local maxima. For example, consider the following fictitious biennial mode, where $n = 5$ and $t_i^{\max}$ are approximately 2 years apart: $t_i^{\max} = \{2002.4, 2004.6, 2006.5, 2008.6, 2010.4\}$. We then apply the following regression model to obtain an "average period", $\omega^{\max}$, and an "average time of maximum", $\varphi^{\max}$, from $t_i^{\max}$: $t_i^{\max} = \omega^{\max} \times (i - [n/2]) + \varphi^{\max}$, where $[x]$ is the integer part of a real number x. In the above example, $\omega^{\max} = 2.0$years and $\varphi^{\max} = 2004.5$. The phase difference between two time series characterizing the temperature at

two levels are thus defined as the difference between the two resultant $\varphi^{\max}$.

Similar calculation for the local minima can also be performed to obtain an average time of minimum $\varphi^{\min}$. In EJME, an ensemble of $\varphi^{\max}$ and $\varphi^{\min}$for each IMF is obtained from the noise-added time series. The ensemble means and the 1-σ standard deviations are shown in Figs. 5, 6, 7, 9; S1–S4.

References

Allen DR, Bevilacqua RM, Nedoluha GE, Randall CE, Manney GL (2003) Unusual stratospheric transport and mixing during the 2002 Antarctic winter. Geophys Res Lett 30:1599. doi:10.1029/2003GL017117

Allen MR, Gillett NP, Kettleborough JA, Hegerl G, Schnur R, Stott PA, Boer G, Covey C, Delworth TL, Jones GS, Mitchell JFB, Barnett TP (2006) Quantifying anthropogenic influence on recent near-surface temperature change. Surv Geophys 27:491–544. doi:10.1007/s10712-006-9011-6

Aumann HH, Chahine MT, Gautier C, Goldberg MD, Kalnay E, McMillin LM, Revercomb H, Rosenkranz PW, Smith WL, Staelin DH, Strow LL, Susskind J (2003) AIRS/AMSU/HSB on the aqua mission: design, science objectives, data products, and processing systems. IEEE Trans Geosci Remote Sens 41:253–264. doi:10.1109/TGRS.2002.808356

Baldwin MP, Tung KK (1994) Extra-tropical QBO signals in angular momentum and wave forcing. Geophys Res Let 21:2717–2720. doi:10.1029/94GL02119

Baldwin MP, Gray LJ, Dunkerton TJ, Hamilton K, Haynes PH, Randel WJ, Holton JR, Alexander MJ, Hirota I, Horinouchi T, Jones DBA, Kinnersley JS, Marquardt C, Sato K, Takahashi M (2001) The quasi-biennial oscillation. Rev Geophys 39:179–229. doi:10.1029/1999RG000073

Bergengren JC, Waliser DE, Yung YL (2011) Ecological sensitivity: a biospheric view of climate change. Clim Chang 107:433–457. doi:10.1007/s10584-011-0065-1

Broecker WS (1975) Climatic change: are we on brink of a pronounced global warming? Science 189:460–463. doi:10.1126/science.189.4201.460

Chen G, Li H (2008) Fine pattern of natural modes in sea surface temperature variability: 1985–2003. J Phys Oceanogr 38:314–336. doi:10.1175/2007JPO3592.1

Christy JR, Norris WB, Spencer RW, Hnilo JJ (2007) Tropospheric temperature change since 1979 from tropical radiosonde and satellite measurements. J Geophys Res Atmos 112:D06102. doi:10.1029/2005JD006881

Daubechies I, Lu JF, Wu HT (2011) Synchrosqueezed wavelet transforms: an empirical mode decomposition-like tool. Appl Comput Harmon Anal 30:243–261. doi:10.1016/j.acha.2010.08.002

Dowdeswell JA, Hagen JO, Bjornsson H, Glazovsky AF, Harrison WD, Holmlund P, Jania J, Koerner RM, Lefauconnier B, Ommanney CSL, Thomas RH (1997) The mass balance of circum-Arctic glaciers and recent climate change. Quat Res 48:1–14. doi:10.1006/qres.1997.1900

Forest CE, Stone PH, Sokolov AP, Allen MR, Webster MD (2002) Quantifying uncertainties in climate system properties with the use of recent climate observations. Science 295:113–117. doi:10.1126/science.1064419

Goldberg MD, Crosby DS, Zhou LH (2001) The limb adjustment of AMSU-A observations: methodology and validation. J Appl Meteorol 40:70–83. doi:10.1175/1520-0450(2001)040<0070:TLAOAA>2.0.CO;2

Goldstein T, Osher S (2009) The split Bregman method for L^1-regularized problems. SIAM J Imaging Sci 2:323–343. doi:10.1137/080725891

Haeberli W, Frauenfelder R, Hoelzle M, Maisch M (1999) On rates and acceleration trends of global glacier mass changes. Geogr Ann Ser A 81:585–591. doi:10.1111/1468-0459.00086

Hirota I (1980) Observational evidence of the semiannual oscillation in the tropical middle atmosphere—a review. Pure Appl Geophys 118:217–238. doi:10.1007/BF01586452

Hou TY, Shi Z (2011) Adaptive data analysis via sparse time–frequency representation. Adv Adapt Data Anal 3:1–28. doi:10.1142/S1793536911000647

Huang NE, Shen Z, Long SR, Wu MLC, Shih HH, Zheng QN, Yen NC, Tung CC, Liu HH (1998) The empirical mode decomposition and the Hilbert spectrum for nonlinear and non-stationary time series analysis. Proc R Soc Lond A 454:903–995. doi:10.1098/rspa.1998.0193

Huang FT, Mayr HG, Reber CA, Russell JM, Mlynczak M, Mengel JG (2006) Stratospheric and mesospheric temperature variations for the quasi-biennial and semiannual (QBO and SAO) oscillations based on measurements from SABER (TIMED) and MLS (UARS). Ann Geophys 24:2131–2149. doi:10.5194/angeo-24-2131-2006

Huang Y, Leroy S, Goody RM (2011) Discriminating between climate observations in terms of their ability to improve an ensemble of climate predictions. Proc Natl Acad Sci USA 108:10405–10409. doi:10.1073/pnas.1107403108

Hughes TP, Baird AH, Bellwood DR, Card M, Connolly SR, Folke C, Grosberg R, Hoegh-Guldberg O, Jackson JBC, Kleypas J, Lough JM, Marshall P, Nystrom M, Palumbi SR, Pandolfi JM, Rosen B, Roughgarden J (2003) Climate change, human impacts, and the resilience of coral reefs. Science 301:929–933. doi:10.1126/science.1085046

IPCC (1990) Climate change: The IPCC scientific assessment. Report prepared for Intergovernmental Panel on Climate Change by Working Group I. In: Houghton JT, Jenkins GJ, Ephraums JJ (eds). Cambridge University Press, Cambridge, Great Britain, 410 pp

IPCC (2007) Climate change 2007: synthesis report. contribution of Working Groups I, II and III to the fourth assessment report of IPCC. In: Core Writing Team, Pachauri RK, Reisinger A (eds). Intergovernmental Panel on Climate Change, Geneva, Switzerland, 104 pp

Jackson DR, Gray LJ (1994) Simulation of the semi-annual oscillation of the equatorial middle atmosphere using the extended UGAMP general-circulation model. Q J R Meteorol Soc 120:1559–1588. doi:10.1002/qj.49712052007

Jiang X, Jones DBA, Shia R, Waliser DE, Yung YL (2005) Spatial patterns and mechanisms of the quasi-biennial oscillation–annual beat of ozone. J Geophys Res Atmos 110:D23308. doi:10.1029/2005JD006055

Jin FF, Kug JS, An SI, Kang IS (2003) A near-annual coupled ocean–atmosphere mode in the equatorial Pacific ocean. Geophys Res Lett 30:1080. doi:10.1029/2002GL015983

Kalnay E, Kanamitsu M, Kistler R, Collins W, Deaven D, Gandin L, Iredell M, Saha S, White G, Woollen J, Zhu Y, Chelliah M, Ebisuzaki W, Higgins W, Janowiak J, Mo KC, Ropelewski C, Wang J, Leetmaa A, Reynolds R, Jenne R, Joseph D (1996) The NCEP/NCAR 40-year reanalysis project. Bull Am Meteorol Soc 77:437–471. doi:10.1175/1520-0477(1996)077<0437:TNYRP>2.0.CO;2

Kang IS, Kug JS, An SI, Jin FF (2004) A near-annual Pacific Ocean basin mode. J Clim 17:2478–2488. doi:10.1175/1520-0442(2004)017<2478:ANPOBM>2.0.CO;2

Keenlyside NS, Latif M, Durkop A (2007) On sub-ENSO variability. J Clim 20:3452–3469. doi:10.1175/JCLI4199.1

Kerr-Munslow AM, Norton WA (2006) Tropical wave driving of the annual cycle in tropical tropopause temperatures. Part I: ECMWF analyses. J Atmos Sci 63:1410–1419. doi:10.1175/JAS3697.1

Kumar KK, Swain D, John SR, Ramkumar G (2011) Simultaneous observations of SAO and QBO in winds, temperature and ozone in the tropical middle atmosphere over Thumba (8.5°N, 77°E). Clim Dyn 37:1961–1973. doi:10.1007/s00382-010-0991-z

L'Ecuyer TS, Jiang JH (2010) Touring the atmosphere aboard the A-train. Phys Today 63:36–41. doi:10.1063/1.3463626

Lambrigtsen BH (2003) Calibration of the AIRS microwave instruments. IEEE Trans Geosci Remote Sens 41:369–378. doi:10.1109/TGRS.2002.808247

Meehl GA (1987) The annual cycle and interannual variability in the tropical Pacific and Indian Ocean regions. Mon Weather Rev 115:27–50. doi:10.1175/1520-0493(1987)115<0027:TACAIV>2.0.CO;2

Meehl GA (1993) A coupled air–sea biennial mechanism in the tropical Indian and Pacific regions: role of the ocean. J Clim 6:31–41. doi:10.1175/1520-0442(1993)006<0031:ACASBM>2.0.CO;2

Meehl GA (1997) The south Asian monsoon and the tropospheric biennial oscillation. J Clim 10:1921–1943. doi:10.1175/1520-0442(1997)010<1921:TSAMAT>2.0.CO;2

Meehl GA, Arblaster JM (2011) Decadal variability of Asian–Australian monsoon–ENSO–TBO relationships. J Clim 24:4925–4940. doi:10.1175/2011JCLI4015.1

Meehl GA, Arblaster JM, Loschnigg J (2003) Coupled ocean–atmosphere dynamical processes in the tropical Indian and Pacific Oceans and the TBO. J Clim 16:2138–2158. doi:10.1175/2767.1

Mo T (2009) A study of the NOAA-15 AMSU-A brightness temperatures from 1998 through 2007. J Geophys Res Atmos 114:D11110. doi:10.1029/2008JD011267

Naujokat B (1986) An update of the observed quasi-biennial oscillation of the stratospheric winds over the tropics. J Atmos Sci 43:1873–1877. doi:10.1175/1520-0469(1986)043<1873:AUOTOQ>2.0.CO;2

Norton WA (2006) Tropical wave driving of the annual cycle in tropical tropopause temperatures. Part II: model results. J Atmos Sci 63:1420–1431. doi:10.1175/JAS3698.1

Olhede S, Walden AT (2004) The Hilbert spectrum via wavelet projections. Proc R Soc Lond A 460:955–975. doi:10.1098/rspa.2003.1199

Pillai PA, Mohankumar K (2010) Individual and combined influence of El Nino–Southern oscillation and Indian Ocean dipole on the tropospheric biennial oscillation. Q J R Meteorol Soc 136:297–304. doi:10.1002/qj.579

Ramanathan V, Crutzen PJ, Kiehl JT, Rosenfeld D (2001) Aerosols, climate, and the hydrological cycle. Science 294:2119–2124. doi:10.1126/science.1064034

Randel WJ, Garcia R, Wu F (2008) Dynamical balances and tropical stratospheric upwelling. J Atmos Sci 65:3584–3595. doi:10.1175/2008JAS2756.1

Randel WJ, Shine KP, Austin J, Barnett J, Claud C, Gillett NP, Keckhut P, Langematz U, Lin R, Long C, Mears C, Miller A, Nash J, Seidel DJ, Thompson DWJ, Wu F, Yoden S (2009) An update of observed stratospheric temperature trends. J Geophys Res Atmos 114:D02107. doi:10.1029/2008JD010421

Rasmusson EM, Carpenter TH (1982) Variations in tropical sea surface temperature and surface wind fields associated with the southern oscillation/El Niño. Mon Weather Rev 110:354–384. doi:10.1175/1520-0493(1982)110<0354:VITSST>2.0.CO;2

Reed RJ, Vlcek CL (1969) The annual temperature variation in the lower tropical stratosphere. J Atmos Sci 26:163–167. doi:10.1175/1520-0469(1969)026<0163:TATVIT>2.0.CO;2

Reynolds RW, Gentemann CL, Corlett GK (2010) Evaluation of AATSR and TMI satellite SST data. J Clim 23:152–165. doi:10.1175/2009JCLI3252.1

Santer BD, Sausen R, Wigley TML, Boyle JS, AchutaRao K, Doutriaux C, Hansen JE, Meehl GA, Roeckner E, Ruedy R, Schmidt G, Taylor KE (2003) Behavior of tropopause height and atmospheric temperature in models, reanalyses, and observations: decadal changes. J Geophys Res Atmos 108:4002. doi:10.1029/2002JD002258

Seidel DJ, Ross RJ, Angell JK, Reid GC (2001) Climatological characteristics of the tropical tropopause as revealed by radiosondes. J Geophys Res Atmos 106:7857–7878. doi:10.1029/2000JD900837

Sela J, Wiin-Nielsen A (1971) Simulation of the atmospheric annual energy cycle. Mon Weather Rev 99:460–468. doi:10.1175/1520-0493(1971)099<0460:SOTAAE>2.3.CO;2

Susskind J, Barnet CD, Blaisdell JM (2003) Retrieval of atmospheric and surface parameters from AIRS/AMSU/HSB data in the presence of clouds. IEEE Trans Geosci Remote Sens 41:390–409. doi:10.1109/TGRS.2002.808236

Taguchi M (2009) Wave driving in the tropical lower stratosphere as simulated by WACCM. Part I: annual cycle. J Atmos Sci 66:2029–2043. doi:10.1175/2009JAS2854.1

Thorne PW, Lanzante JR, Peterson TC, Seidel DJ, Shine KP (2011) Tropospheric temperature trends: history of an ongoing controversy. Wiley Interdiscip Rev Clim Chang 2:66–88. doi:10.1002/wcc.80

Tomita T, Yasunari T (1996) Role of the northeast winter monsoon on the biennial oscillation of the ENSO/monsoon system. J Meteorol Soc Jpn 74:399–413

Tung KK, Yang H (1994) Global QBO in circulation and ozone. Part I: reexamination of observational evidence. J Atmos Sc 51:2699–2707. doi:10.1175/1520-0469(1994)051<2699:GQICAO>2.0.CO;2

Wang CZ, Picaut J (2004) Understanding ENSO physics—a review. In: Wang C, Xie S-P, Carton JA (eds) Earth's climate: the ocean–atmosphere interaction, Geophys Monogr Ser, vol 147. AGU, Washington, DC, pp 21–48. doi:10.1029/GM147

Wigley TML, Raper SCB (1992) Implications for climate and sea level of revised IPCC emissions scenarios. Nature 357:293–300. doi:10.1038/357293a0

Wolter K, Timlin MS (2011) El Niño/southern oscillation behaviour since 1871 as diagnosed in an extended multivariate ENSO index (MEI.ext). Int J Climatol 31:1074–1087. doi:10.1002/joc.2336

Wu Z, Huang NE (2009) Ensemble empirical mode decomposition: a noise-assisted data analysis method. Adv Adapt Data Anal 1:1–41. doi:10.1142/S1793536909000047

Wu H-T, Flandrin P, Daubechies I (2011) One or two frequencies? The synchrosqueezing answers. Adv Adapt Data Anal 3:29–39. doi:10.1142/S179353691100074X

Xu J, Powell AM Jr (2012) Uncertainty estimation of the global temperature trends for multiple radiosondes, reanalyses, and CMIP3/IPCC climate model simulations. Theor Appl Climatol 108:505–518. doi:10.1007/s00704-011-0548-z

Yoshida K, Yamazaki K (2011) Tropical cooling in the case of stratospheric sudden warming in January 2009: focus on the tropical tropopause layer. Atmos Chem Phys 11:6325–6336. doi:10.5194/acp-11-6325-2011